

## Morphological modeling using a fully coupled, total variation diminishing upwind-biased centered scheme

Wei Li,<sup>1</sup> Huib J. de Vriend,<sup>1,2</sup> Zhengbing Wang,<sup>1,2</sup> and D. S. van Maren<sup>1,2</sup>

Received 12 June 2012; revised 8 February 2013; accepted 9 February 2013.

[1] High-resolution morphological modeling of fluvial processes with complex, rapidly varying flows has been limited so far by model accuracy or computational efficiency. One of the most widely used numerical algorithms is based on the total variation diminishing method, solved by either upwind or centered approaches. An upwind scheme preserves high accuracy but is complex and computationally demanding, whereas the simplicity and efficiency of a centered approach compromise the accuracy. The present paper extends a recent upwind-biased centered scheme originally developed for clear water and scalar transport over a rigid bed, to sediment-laden flows over an erodible bed. It does so by developing a fully coupled 2-D mathematical model using a finite volume method for structured grids. The complete set of noncapacity-based governing equations, involving the effects of bed deformation and sediment density variation, as well as the influences of turbulence and sediment diffusion, and the temporal and spatial scales needed for sediment adaptation, is solved at one time to obtain synchronous solutions for the entire computational domain. For stability, a two-stage splitting approach together with a second-order Runge-Kutta method is employed for the source terms. The model is verified in a number of tests covering a wide range of complex (sediment-laden) flows. The model is demonstrated to accurately simulate shock waves and reflection waves, but also rapid bed deformations at high sediment transport rates. The combination of high numerical accuracy and computational efficiency makes the model an important tool to forecast flood events in morphologically complex areas.

**Citation:** Li, W., H. J. de Vriend, Z. Wang, and D. S. van Maren (2013), Morphological modeling using a fully coupled, total variation diminishing upwind-biased centered scheme, *Water Resour. Res.*, 49, doi:10.1002/wrcr.20138.

### 1. Introduction

[2] Turbulent flows (including wind, open-channel flow, pipe flow, and subaqueous flow) over an erodible bed generate sediment transport and morphological changes, which in turn influence the flow. In addition to laboratory experiments and field surveys, mathematical modeling approach has become increasingly popular for studying morphological change due to sediment transport. In this paper we will show the development and validation of a morphological model for open-channel flow, taking into account of the latest progresses on both the physical process of sediment transport by water flow and the numerical approach used in solving the equations.

[3] According to the different way the physical process of sediment transport is dealt with, morphological models

can be coupled or decoupled, with a capacity or noncapacity transport formulation [e.g., *Cao et al.*, 2012]. In a capacity model, sediment transport is assumed to be always in equilibrium with the local flow conditions, whereas a noncapacity model is more physically advanced as it includes the spatial and temporal lag effects. By the term “coupled” and “decoupled,” we follow the philosophy of *Cao et al.* [2012]. In a decoupled model [e.g., *Cunge et al.*, 1980; *Cui et al.*, 1996; *Sieben*, 1999; *Di Cristo et al.*, 2006], the effects of sediment density and bed deformation on the flow are neglected, whereas a fully coupled model incorporates those effects into the flow mass and momentum conservation. A partially coupled model [*Phillips and Sutherland*, 1989; *Capart and Young*, 1998; *Fraccarollo and Capart*, 2002; *Lesser et al.*, 2004; *Rosatti and Fraccarollo*, 2006; *Canestrelli et al.*, 2010; *Garegnani et al.*, 2011] falls in between the decoupled and fully coupled models. A decoupled or partially coupled model is applicable only in the cases for which the timescale of morphological change is much longer than that of the flow adaptation to a changing bed topography [*Cao et al.*, 2007; *Hu and Cao*, 2009]. Otherwise, a fully coupled model is warranted. In the present paper, we employ the approach of fully coupled noncapacity model to incorporate as much physics as possible. This is important because for highly concentrated floods with rapid morphological change, the sediment-induced density effects and bed

<sup>1</sup>Department of Hydraulic Engineering, Faculty of Civil Engineering and Geosciences, Delft University of Technology, Delft, Netherlands.

<sup>2</sup>Deltares, Delft, Netherlands.

Corresponding author: W. Li, Department of Hydraulic Engineering, Faculty of Civil Engineering and Geosciences, Delft University of Technology, PO Box 5048, NL-2600 GA Delft, Netherlands. (lwpiglet@hotmail.com)

deformation influence are so important that the decoupled or partially coupled models cannot adequately take account of all important physical processes. This is exemplified by a number of recently developed fully coupled noncapacity models [Egashira *et al.*, 2001; Cao *et al.*, 2004; Simpson and Castellort, 2006; Wu and Wang, 2008; Hu and Cao, 2009; Xia *et al.*, 2010; Li and Duffy, 2011; Hu *et al.*, 2012].

[4] Another key issue on resolving the complex processes of morphological change is related to the numerical scheme used for solving the governing equations, which lacks sufficient improvement from the perspective of the state-of-the-art progress in numerical schemes. Generally, the complexity of the fluvial processes requires robust and accurate numerical schemes. This includes tracking of the wet/dry front, capturing shock waves between supercritical and subcritical flow regimes and contact discontinuities (i.e., steep sediment concentration gradients), and accurately conserving water and sediment mass. Total variation diminishing (TVD) versions of the finite volume method (FVM) have been widely used in mathematical modeling of shallow water flows in the last two decades [Alcrudo and Garcia-Navarro, 1993; Toro, 2001; Bradford and Sanders, 2002; Cao *et al.*, 2004; Hu and Cao, 2009; Xia *et al.*, 2010; Wu *et al.*, 2012]. They are attractive because of (1) their ability to automatically capture shock waves and (2) the incorporation of a simple wetting/drying procedure enabling to track wet/dry fronts. Most TVD algorithms, however, take either an upwind approach represented by Godunov [1959] type methods, such as the widely used Roe approximate solver, HLL (Harten-Lax-van Leer), HLLC (Harten-Lax-van Leer-Contact) method [Roe, 1981; Toro, 2001], or a centered approach based on the Lax-Friedrichs method [Lax, 1954], such as FLIC (Flux Limiter Centered) or SLIC (Slope Limiter Centered) [Toro, 2001; Hu *et al.*, 2012]. Upwind methods produce highly accurate numerical results as they use local flow information, but they are complex and computationally expensive. Centered methods, on the other hand, can enhance the computational efficiency considerably and are much simpler to apply to complicated set of equations, but they may significantly compromise accuracy, especially in case of small Courant numbers and contact discontinuities. Fortunately, the high accuracy of an upwind scheme and the computational efficiency of a centered scheme were recently combined in an “upwind-biased FORCE (First Order Centered) method (UFORCE)” based on the FVM for structured meshes [Stecca *et al.*, 2010]. This fantastic method, however, has been not yet applied to mobile-bed processes.

[5] The aim of this paper is to extend the second-order version of the UFORCE to sediment-laden flows over a mobile bed under the framework of the fully coupled noncapacity modeling approach. The model’s capabilities to accurately capture shock waves and dry-wet fronts and predict sediment transport and rapid morphological change are demonstrated by five test cases. The present work is an important step forward in attaining high accuracy and efficient modeling of complex morphodynamics. First, in natural rivers the computational domain is usually large and hence requires a highly efficient computational procedure. Second, the effects of high sediment concentrations and rapid bed deformations (such as in mobile-bed dam-break flows and during highly sediment-laden floods in the Yellow River, China) require a numerical accuracy that is often insufficient

in existing morphological models. Third, the spatial and temporal lag effects of sediment transport can be important to morphological change and thus need a noncapacity modeling framework to incorporate as much physics as possible.

## 2. Mathematical Model

### 2.1. Governing Equations

[6] Based on the concept of noncapacity sediment transport, the nonlinear system of governing equations for the 2-D coupled mathematical model consists of the mass and momentum conservation equations for sediment-laden flow, the mass conservation equation for the sediment, and a bed update equation:

$$\frac{\partial(\rho h)}{\partial t} + \frac{\partial(\rho hu)}{\partial x} + \frac{\partial(\rho hv)}{\partial y} = -\frac{\partial(\rho_0 z)}{\partial t} + \rho_s \Phi_s \quad (1)$$

$$\begin{aligned} \frac{\partial(\rho hu)}{\partial t} + \frac{\partial(\rho hu^2 + 0.5\rho gh^2)}{\partial x} + \frac{\partial(\rho huv)}{\partial y} \\ = \rho gh(S_{0x} - S_{fx}) + \rho \frac{\partial(h\tau_{xx})}{\partial x} + \rho \frac{\partial(h\tau_{xy})}{\partial y} \end{aligned} \quad (2)$$

$$\begin{aligned} \frac{\partial(\rho hv)}{\partial t} + \frac{\partial(\rho huv)}{\partial x} + \frac{\partial(\rho hv^2 + 0.5\rho gh^2)}{\partial y} \\ = \rho gh(S_{0y} - S_{fy}) + \rho \frac{\partial(h\tau_{yx})}{\partial x} + \rho \frac{\partial(h\tau_{yy})}{\partial y} \end{aligned} \quad (3)$$

$$\frac{\partial(hc)}{\partial t} + \frac{\partial(huc)}{\partial x} + \frac{\partial(hvc)}{\partial y} = (E - D) + \Phi_s \quad (4)$$

$$(1 - p) \frac{\partial z}{\partial t} = D - E, \quad (5)$$

where  $t$  is the time;  $x$  and  $y$  are the horizontal coordinates;  $h$  is the water depth;  $u$  and  $v$  are the depth-averaged flow velocities in  $x$  and  $y$  directions, respectively;  $c$  is the depth-averaged volumetric sediment concentration;  $z$  is the bed elevation;  $E$  and  $D$  are the sediment entrainment and deposition fluxes, respectively;  $\tau_{xx}$ ,  $\tau_{yy}$ ,  $\tau_{xy}$ , and  $\tau_{yx}$  are the depth-averaged Reynolds stresses, expressed as  $\tau_{xx} = 2\nu_t \partial u / \partial x$ ,  $\tau_{yy} = 2\nu_t \partial v / \partial y$ ,  $\tau_{xy} = \tau_{yx} = \nu_t (\partial u / \partial y + \partial v / \partial x)$ ;  $\nu_t$  is the turbulent eddy viscosity;  $\Phi_s = \partial(h\varepsilon_s \partial c / \partial x) / \partial x + \partial(h\varepsilon_s \partial c / \partial y) / \partial y$  is the sediment diffusion terms;  $\varepsilon_s$  is the turbulent diffusion coefficient of sediment;  $S_{0x}$  and  $S_{0y}$  are the bed slopes in  $x$  and  $y$  directions, expressed as  $S_{0x} = -\partial z / \partial x$ ,  $S_{0y} = -\partial z / \partial y$  and respectively;  $S_{fx}$ ,  $S_{fy}$  are the friction slopes in  $x$  and  $y$  directions, respectively;  $\rho_s$  is the sediment density;  $\rho_w$  is the water density;  $\rho = \rho_w(1 - c) + \rho_s c$  is the density of sediment-laden flow;  $\rho_0 = \rho_w p + \rho_s(1 - p)$  is the density of saturated bed;  $p$  is the bed porosity; and  $g$  is the acceleration of gravity.

[7] Physically, sediment diffusion exists due to turbulent mixing processes [Julien, 2010]. Together with the advection process, it may contribute to the sediment mass variation, and therefore to the mass variation of the sediment-laden flow. In some multiphase models, the sediment diffusion effect has been considered in the mass conservation of sediment load, though neglected in that of the sediment-laden flow [Lesser *et al.*, 2004; Xia *et al.*, 2010]. Its

complete absence in most other models (in the mass conservation of both the moving sediment and the water-sediment mixture) is due to its negligible influence in most conditions for which advection always dominates. Yet diffusion would be important in conditions such as overbank flows. To incorporate more well-understood physical processes in the mathematical formulations, the sediment diffusion effect is fully considered in the present model in the mass conservation of not only the moving sediment, but also the water-sediment mixture.

## 2.2. Empirical Relationships

[8] Empirical relationships are deployed to close the above governing equations. In the test cases treated herein, the friction slope is estimated by Manning roughness coefficient  $n$ , as

$$S_{fx} = \frac{n^2 u \sqrt{u^2 + v^2}}{h^{4/3}}, \quad (6a)$$

$$S_{fy} = \frac{n^2 v \sqrt{u^2 + v^2}}{h^{4/3}}. \quad (6b)$$

[9] For the noncapacity sediment transport, an empirical coefficient  $\alpha$  is used to estimate the sediment exchange flux with the bed (see equations (7a) and (7b)) following *Cao et al.*'s [2004] method. This is equivalent to the method of the adaptation length for sediment lag effects in previous studies [*Phillips and Sutherland*, 1989; *Wu et al.*, 2000]. Physically, the coefficient  $\alpha$  denotes the ratio of the near-bed to depth-averaged concentrations and should be usually larger than unity. To date, there has been no consensus on its value. In the present work, constant values of the coefficient  $\alpha$  are specified in the simulation, but they differ case by case. The sediment entrainment and deposition are estimated as

$$E = \alpha \omega c_e, \quad (7a)$$

$$D = \alpha \omega c, \quad (7b)$$

where  $c_e$  is the depth-averaged sediment transport capacity, and  $\omega$  is the sediment settling velocity (m/s). In the test cases, the sediment is relatively coarse (viz., natural sand or artificial pearls), and the hindered settling effect is negligible. Thus, the formulation of sediment settling velocity in the clear water condition is used [*Zhang and Xie*, 1993]. The (depth-averaged) sediment transport capacity is calculated by the *Meyer-Peter and Müller* [1948] formula with a modified parameter  $\varphi$ , as indicated in the following equation:

$$q_b = \varphi 8 \sqrt{sgd^3} (\theta - \theta_c)^{1.5}, \quad (8a)$$

$$c_e = \frac{q_b}{(h \sqrt{u^2 + v^2})}, \quad (8b)$$

where  $q_b$  is the bed load transport rate under capacity state ( $m^2/s$ ),  $\varphi$  is the modified parameter,  $s$  is the submerged specific gravity of sediment ( $\rho_s/\rho_w - 1$ ),  $\theta = u_*^2/sgd$  is the Shields parameter,  $u_*$  is the friction velocity,  $\theta_c$  is the

threshold Shields parameter, and  $d$  is the sediment diameter (m). Other parameters are the same as specified earlier.

## 3. Numerical Method

[10] Using a FVM, the full set of the governing equations is rewritten in a conservative form and solved explicitly by a synchronous solution for structured grids. The key problem for computing advection of strong spatial gradients in sediment-laden flows is tackled with the successful extension of the second-order UFORCE scheme [*Stecca et al.*, 2010] from an idealized frictionless-fixed bed to a movable bed. For stability, the two-step splitting approach [*Toro*, 2001] is employed combined with a second-order Runge-Kutta method for source terms [*Toro*, 2009]. The model is second-order accurate in space and time. The time step is restricted by the Courant-Friedrichs-Lewy (CFL) condition and additional conditions relevant to the sediment transport and bed change computations. Wetting and drying fronts are treated using two tolerance depths for the cell type judgment [*Zhao et al.*, 1994]. For open boundaries, a modified characteristic method is adopted, which uses the above Runge-Kutta method and considers morphological update in each iteration cycle. This permits a synchronous solution for the entire computational domain. A free-slip and nonpermeable condition is used for closed walls.

### 3.1. Conservative Form of the Governing Equations

[11] Following *Cao et al.* [2004], the governing equations for the sediment-laden flow are manipulated in a conservative form with the influences of flow density variation and the bed deformation contribution to the flow appearing in the source terms. It results in a simple format of the advection term that permits an easy extension of any high-resolution FVM previously developed for shallow flows over a fixed bed to a mobile bed. To achieve a synchronous solution for the full equation set, further mathematical treatment [*Zhang and Xie*, 1993; *Li and Duffy*, 2011] is used in deriving the conservative form. The bed update equation is replaced by a newly constructed equation (i.e., the fifth equation of the vector form equations (9), (10a), (10b), (10c), (11a), and (11b) of the governing equations). This equation is acquired by summing equations (4) and (5). Physically, it indicates that the variation of sediment mass (including the sediment in motion and the static sediment in bed) in time depends on the effects of advection and diffusion. Furthermore, this treatment ensures a uniform way in the numerical solution of the sediment-laden flow and bed deformation, which avoids the possible mass balance error when applying different numerical schemes for those processes. Thus, the vector form of the governing equations reads

$$\frac{\partial \mathbf{U}}{\partial t} + \frac{\partial \mathbf{F}}{\partial x} + \frac{\partial \mathbf{G}}{\partial y} = \mathbf{H} + \mathbf{I}, \quad (9)$$

$$\mathbf{U} = \begin{bmatrix} h \\ hu \\ hv \\ hc \\ \phi \end{bmatrix}, \quad (10a)$$

$$\mathbf{F} = \begin{bmatrix} hu \\ hu^2 + 0.5gh^2 \\ huv \\ huc \\ huc \end{bmatrix}, \quad (10b)$$

$$\mathbf{G} = \begin{bmatrix} hv \\ hvu \\ hv^2 + 0.5gh^2 \\ hvc \\ hvc \end{bmatrix}, \quad (10c)$$

$$\mathbf{H} = \begin{bmatrix} \frac{E-D}{1-p} \\ gh(S_{0x} - S_{fx}) - \frac{(\rho_s - \rho_w)gh^2}{2\rho} \frac{\partial c}{\partial x} - \frac{(\rho_0 - \rho)(E-D)u}{\rho(1-p)} \\ gh(S_{0y} - S_{fy}) - \frac{(\rho_s - \rho_w)gh^2}{2\rho} \frac{\partial c}{\partial y} - \frac{(\rho_0 - \rho)(E-D)v}{\rho(1-p)} \\ E-D \\ 0 \end{bmatrix} \quad (11a)$$

$$\mathbf{I} = \begin{bmatrix} \Phi_s \\ \frac{\partial(h\tau_{xx})}{\partial x} + \frac{\partial(h\tau_{xy})}{\partial y} - \frac{\rho_s - \rho_w}{\rho} u(1-c)\Phi_s \\ \frac{\partial(h\tau_{yx})}{\partial x} + \frac{\partial(h\tau_{yy})}{\partial y} - \frac{\rho_s - \rho_w}{\rho} v(1-c)\Phi_s \\ \Phi_s \\ \Phi_s \end{bmatrix} \quad (11b)$$

where  $\mathbf{U}$  is the vector of conservative variables,  $\mathbf{F}$  and  $\mathbf{G}$  are the vectors of flux variables,  $\mathbf{H}$  is the vector of source terms,  $\mathbf{I}$  is the vector of diffusive terms, and  $\phi = (1-p)z + hc$  is the newly constructed conservative variable.

### 3.2. Discretization of the Governing Equations

[12] For solving the governing equations, the computational domain is divided into a structured set of quadrilateral cells. A cell-centered FVM is adopted in the model, with the average values of conserved variables being defined at the center and interfaces at the edges. Integrating equation (9) within a control volume  $(i, j)$  and applying the divergence theorem, we can get the discretized equation in the Cartesian  $x$  and  $y$  coordinates:

$$\begin{aligned} \frac{\partial \mathbf{U}_{ij}}{\partial t} + \frac{1}{\Delta x} (\mathbf{F}_{i+1/2,j}(\mathbf{U}) - \mathbf{F}_{i-1/2,j}(\mathbf{U})) \\ + \frac{1}{\Delta y} (\mathbf{G}_{i,j+1/2}(\mathbf{U}) - \mathbf{G}_{i,j-1/2}(\mathbf{U})) = \mathbf{R}(\mathbf{U}_{ij}), \end{aligned} \quad (12)$$

where  $\Delta x$  and  $\Delta y$  are the spatial steps in  $x$  and  $y$  directions;  $i$  and  $j$  are the cell indices in  $x$  and  $y$  directions;  $\mathbf{U}_{ij}$  is the vector of cell-averaged conservative variable at the center;  $\mathbf{R} = \mathbf{H} + \mathbf{I}$  is the vector of total source terms; and  $\mathbf{F}_{i+1/2,j}(\mathbf{U})$ ,  $\mathbf{F}_{i-1/2,j}(\mathbf{U})$ ,  $\mathbf{G}_{i,j+1/2}(\mathbf{U})$ , and  $\mathbf{G}_{i,j-1/2}(\mathbf{U})$  are the vectors of normal flux at interfaces  $(i+1/2, j)$ ,  $(i-1/2, j)$ ,  $(i, j+1/2)$ , and  $(i, j-1/2)$ , respectively. The fluxes are computed using the second-order UFORCE scheme in the  $x$  and  $y$  directions, respectively (see section 3.4). The spatial

gradients of bed level and sediment concentration in the source terms are discretized in an upwind manner for stability.

### 3.3. Method of Time Integration

[13] A standard splitting approach [Toro, 2001] is deployed to solve the inhomogeneous system of equation (12). In this approach, the homogeneous equation (13) is solved first, of which the intermediate result is used for the ordinary equation related to source term. For stability, a second-order Runge-Kutta method [Toro, 2009] is used in computing the ordinary equation (14). The overall accuracy in time is supposed to reach second order by approximating the source term and advection flux with second-order schemes. The solution procedure for the splitting approach is illustrated by the following equations:

$$\begin{aligned} \mathbf{U}_{ij}^* = \mathbf{U}_{ij}^n - \frac{\Delta t}{\Delta x} (\mathbf{F}_{i+1/2,j}(\mathbf{U}^n) - \mathbf{F}_{i-1/2,j}(\mathbf{U}^n)) \\ - \frac{\Delta t}{\Delta y} (\mathbf{G}_{i,j+1/2}(\mathbf{U}^n) - \mathbf{G}_{i,j-1/2}(\mathbf{U}^n)), \end{aligned} \quad (13)$$

$$\mathbf{U}_{ij}^{n+1} = \mathbf{U}_{ij}^* + 0.5(\mathbf{K}_1 + \mathbf{K}_2), \quad (14)$$

with

$$\mathbf{K}_1 = \Delta t \mathbf{R}(\mathbf{U}_{ij}^*), \quad \mathbf{K}_2 = \Delta t \mathbf{R}(\mathbf{U}_{ij}^* + \mathbf{K}_1), \quad (15)$$

where  $\mathbf{U}_{ij}^*$  is the vector of predictor variables at the intermediate stage;  $\mathbf{U}_{ij}^n$  and  $\mathbf{U}_{ij}^{n+1}$  are the vectors of conservative variables at the time steps  $n$  and  $n+1$ , respectively; and  $\Delta t$  is the computational time step.

[14] Because the solution procedure is explicit, the computational time step should be restricted by stability conditions. For flow computation, the time restriction mainly results from the advection term (i.e., in flow field) and the diffusion term (i.e., in geometrical domain). The former can be described by the CFL condition (16) and the latter by the stability condition (17) related to the Peclet number  $Pe$  (i.e.,  $0 < Pe = 2\nu_t \Delta t / \Delta x^2 \leq 1$ ). For advection-dominated problems, the CFL condition plays a major role in controlling the flow computation. While in diffusion-dominated problems with very fine computational grids, the Peclet number may strongly restrict the time step.

$$\Delta t_f \leq \frac{Cr}{\max[ (|u| + \sqrt{gh}) / \Delta x, (|v| + \sqrt{gh}) / \Delta y ]}, \quad (16)$$

where  $\Delta t_f$  is the time step related to CFL condition, and  $Cr$  is the Courant number ( $0 < Cr \leq 1$ ).

$$\Delta t_g \leq \frac{1}{\max(2\nu_t / \Delta x^2, 2\nu_t / \Delta y^2)}, \quad (17)$$

where  $\Delta t_g$  is the time step related to Peclet number condition.

[15] For sediment transport and bed change, additional condition (18) is used, ensuring the amount of deposited

sediment within a time step less than that in the flow (i.e.,  $\Delta t_s D \leq hc$ ), which is similar to that by *Heng et al.* [2009],

$$\Delta t_s \leq \frac{h}{\alpha \omega}, \quad (18)$$

where  $\Delta t_s$  is the time step related to the mobile-bed condition.

[16] Exact expressions of stability conditions for the whole complex system are difficult to derive. We choose the most restrictive option from the above conditions (see equation (19)). The applicability of this method is demonstrated by the satisfactory results in the model testing below.

$$\Delta t = \min(\Delta t_f, \Delta t_g, \Delta t_s). \quad (19)$$

### 3.4. UFORCE Scheme for Computing Fluxes

[17] The UFORCE scheme [Stecca et al., 2010] is an upwind-biased version of the FORCE scheme [Toro, 2009], which requires a primary (Cartesian) mesh to compute cell-averaged variables and four staggered (non-Cartesian) meshes for computing interface fluxes in 2-D conditions. An upwind bias parameter is introduced by modifying the shape of the staggered mesh from the original Cartesian shape of the FORCE scheme in the  $x$  and  $y$  directions, respectively. The UFORCE scheme has been demonstrated to be capable of accurately capturing shock waves and contact discontinuities for shallow water flow and scalar transport over a rigid bed without source terms. Here the second-order version of this scheme, which is constructed through the MUSCL (Monotonic Upstream-Centered Scheme for Conservation Laws)-Hancock approach [Van Leer, 1979], is extended for the computation of sediment-laden flows over a mobile bed. Three steps are involved: (1) spatially second-order accuracy by data reconstruction; (2) temporally second-order accuracy by state evolution; and (3) computation of UFORCE flux (viz., solve the Riemann problem). In the following, the extension procedure is introduced for the computation of advection flux in  $x$  direction, for instance. In  $y$  direction, analogous method is employed.

#### 3.4.1. MUSCL Reconstruction

[18] To reach second-order accuracy in space, the cell interface values are extrapolated from the cell center values by a limited slope,

$$\mathbf{U}_{i+1/2,j}^L = \mathbf{U}_{ij}^n + 0.5\overline{\Delta}_i, \quad \mathbf{U}_{i+1/2,j}^R = \mathbf{U}_{i+1,j}^n - 0.5\overline{\Delta}_{i+1}, \quad (20)$$

where  $\mathbf{U}_{i+1/2,j}^L$ ,  $\mathbf{U}_{i+1/2,j}^R$  are the vectors of extrapolated variables at the left and right sides of the interface between cells  $(i,j)$  and  $(i+1,j)$ ; and  $\overline{\Delta}_i$  and  $\overline{\Delta}_{i+1}$  are the vectors of

limited slope. Many methods have been introduced to construct the limited slope and slope limiters for TVD schemes. Here it is computed by the ENO (Essentially Non Oscillatory) approach [Harten et al., 1987] to avoid spurious oscillations near large gradients [Stecca et al., 2010],

$$\overline{\Delta}_i = \begin{cases} \mathbf{U}_{i+1,j}^n - \mathbf{U}_{i,j}^n & \text{if } |\mathbf{U}_{i+1,j}^n - \mathbf{U}_{i,j}^n| \leq \mathbf{U}_{i,j}^n - \mathbf{U}_{i-1,j}^n \\ \mathbf{U}_{i,j}^n - \mathbf{U}_{i-1,j}^n & \text{otherwise} \end{cases}. \quad (21)$$

#### 3.4.2. State Evolution by $\Delta t/2$

[19] The cell interface variables are further evolved over a half time step to reach second-order accuracy in time, as

$$\begin{aligned} \mathbf{U}_{i+1/2,j}^{L*} &= \mathbf{U}_{i+1/2,j}^L + \frac{\Delta t}{2\Delta x} \left[ \mathbf{F}(\mathbf{U}_{i-1/2,j}^R) - \mathbf{F}(\mathbf{U}_{i+1/2,j}^L) \right] \\ &+ \frac{\Delta t}{2\Delta y} \left[ \mathbf{G}(\mathbf{U}_{i,j-1/2}^R) - \mathbf{G}(\mathbf{U}_{i,j+1/2}^L) \right] \end{aligned} \quad (22a)$$

$$\begin{aligned} \mathbf{U}_{i+1/2,j}^{R*} &= \mathbf{U}_{i+1/2,j}^R + \frac{\Delta t}{2\Delta x} \left[ \mathbf{F}(\mathbf{U}_{i+1/2,j}^R) - \mathbf{F}(\mathbf{U}_{i+3/2,j}^L) \right] \\ &+ \frac{\Delta t}{2\Delta y} \left[ \mathbf{G}(\mathbf{U}_{i+1,j-1/2}^R) - \mathbf{G}(\mathbf{U}_{i+1,j+1/2}^L) \right]. \end{aligned} \quad (22b)$$

#### 3.4.3. UFORCE Flux Computation (i.e., Riemann Problem)

[20] At the interface  $(i+1/2,j)$ , a pair of constant states  $(\mathbf{U}_{i+1/2,j}^{L*}, \mathbf{U}_{i+1/2,j}^{R*})$  has been obtained from the above steps. The advection flux can now be computed by the UFORCE scheme, which is essentially an average of the upwind-biased versions of the Lax-Friedrichs flux and the two-step Lax-Wendroff flux, as

$$\mathbf{F}_{i+1/2,j}^{\text{UFORCE } \alpha_D} = 0.5 \left( \mathbf{F}_{i+1/2,j}^{\text{uLW } \alpha_D} + \mathbf{F}_{i+1/2,j}^{\text{uLF } \alpha_D} \right), \quad (23)$$

where  $\alpha_D$  is the number of dimensions, i.e., =1 for 1-D case, =2 for 2-D case;  $\mathbf{F}_{i+1/2,j}^{\text{uLW } \alpha_D}$  is the upwind-biased version of the two-step Lax-Wendroff flux;  $\mathbf{F}_{i+1/2,j}^{\text{uLF } \alpha_D}$  is the upwind-biased version of the Lax-Friedrichs flux;  $\mathbf{F}_{i+1/2,j}^{\text{UFORCE } \alpha_D}$  is the UFORCE flux.

[21] The upwind-biased Lax-Wendroff flux is estimated by introducing an upwind bias parameter  $\beta$  in the original Lax-Wendroff flux [Toro, 2009], like

$$\mathbf{F}_{i+1/2,j}^{\text{uLW } \alpha_D} = \mathbf{F}(\mathbf{U}_{i+1/2,j}^{\text{uLW } \alpha_D}) \quad (24a)$$

$$\mathbf{U}_{i+1/2,j}^{\text{uLW } \alpha_D} = \frac{\left(1 + 2(\beta_x)_{ij}\right) \mathbf{U}_{i+1/2,j}^{L*} + \left(1 - 2(\beta_x)_{i+1,j}\right) \mathbf{U}_{i+1/2,j}^{R*} - \frac{\alpha_D \Delta t}{\Delta x} \left( \mathbf{F}(\mathbf{U}_{i+1/2,j}^{R*}) - \mathbf{F}(\mathbf{U}_{i+1/2,j}^{L*}) \right)}{2 \left(1 - (\beta_x)_{i+1,j} + (\beta_x)_{ij}\right)}, \quad (24b)$$

where  $\mathbf{U}_{i+1/2,j}^{\text{uLW } \alpha_D}$  is the vector of newly constructed conservative variable in the two-step Lax-Wendroff flux;  $\alpha_D$  is the number of dimensions, i.e., =1 for 1-D case, =2 for 2-D

case; and  $\beta_x$  is the upwind bias parameter in  $x$  direction. The upwind-biased Lax-Friedrichs flux is estimated by [Stecca et al., 2010]

$$\mathbf{F}_{i+1/2,j}^{\text{uLF}\alpha_D} = \frac{1}{2(1 - (\beta_x)_{i+1,j} + (\beta_x)_{i,j})} \left[ \left( (1 + 2(\beta_x)_{i,j}) \mathbf{F}(\mathbf{U}_{i+1/2,j}^{R*}) + (1 - 2(\beta_x)_{i+1,j}) \mathbf{F}(\mathbf{U}_{i+1/2,j}^{L*}) \right) - \frac{\Delta x}{\alpha_D \Delta t} (1 + 2(\beta_x)_{i,j}) (1 - 2(\beta_x)_{i+1,j}) (\mathbf{U}_{i+1/2,j}^{R*} - \mathbf{U}_{i+1/2,j}^{L*}) \right] \quad (25)$$

[22] The critical issue in the extension to the mobile-bed case therefore relates to the estimation of the upwind bias parameter. In shallow water flows, this parameter is computed separately in  $x$  and  $y$  directions but use the same method [Stecca *et al.*, 2010]. For the parameter in the  $x$  direction, we use

$$(\beta_x)_{i,j} = \text{SIG}_{i,j} \left( 0.5 - \lambda_{\text{sx}} \frac{\Delta t}{\Delta x} \right)_{i,j} \quad (26)$$

with function

$$\text{SIG}_{i,j} = \begin{cases} \text{sign}(u_{i,j}) & \text{if } (u_{i,j} \neq 0) \\ \text{sign}((\lambda_3)_{i-1,j} + (\lambda_1)_{i+1,j}) & \text{if } (u_{i,j} = 0) \text{ and } (\lambda_3)_{i-1,j} + (\lambda_1)_{i+1,j} \neq 0 \\ 0 & \text{if } (u_{i,j} = 0) \text{ and } (\lambda_3)_{i-1,j} + (\lambda_1)_{i+1,j} = 0 \end{cases} \quad (27)$$

$$\text{sign}(u_{i,j}) = \begin{cases} 1 & \text{if } u_{i,j} > 0 \\ -1 & \text{if } u_{i,j} < 0 \end{cases} \quad (28)$$

where  $\lambda_{\text{sx}}$  is the absolute value of the maximum local characteristic speed in shallow water flows; and  $\lambda_{1,3}$  is the characteristic speed related to the flow part. For the fixed bed case, the values of the characteristic speed are [Stecca *et al.*, 2010]

$$\lambda_{\text{sx}} = (|u| + \sqrt{gh})_{i,j}, \quad (29a)$$

$$\lambda_1 = u - \sqrt{gh}, \quad (29b)$$

$$\lambda_3 = u + \sqrt{gh}. \quad (29c)$$

[23] In the extension to the mobile bed, the values of the characteristic speed can be estimated by rewriting the equation system in a nonconservative form. In 1-D problem, the nonconservative vector form of the governing equations for our model reads (i.e., in  $x$  direction)

$$\frac{\partial \mathbf{W}}{\partial t} + \mathbf{A} \frac{\partial \mathbf{W}}{\partial x} = \mathbf{R}' \quad (30)$$

$$\mathbf{W} = \begin{bmatrix} h \\ u \\ c \\ (1-p)z + c \end{bmatrix}, \quad (31a)$$

$$\mathbf{A} = \begin{bmatrix} u & h & 0 & 0 \\ g & u & a_{23} & a_{24} \\ 0 & 0 & u & 0 \\ 0 & 0 & u & 0 \end{bmatrix}, \quad (31b)$$

$$\mathbf{R}' = \begin{bmatrix} R'_1 \\ R'_2 \\ R'_3 \\ R'_4 \end{bmatrix} = \begin{bmatrix} \frac{E-D}{1-p} + \Phi_{\text{sx}} \\ -gS_{\text{fx}} - \frac{\rho_0 u (E-D)}{\rho h (1-p)} - \frac{\rho_s u}{\rho h} \Phi_{\text{sx}} + \frac{1}{h} \frac{\partial (h\tau_{\text{xx}})}{\partial x} \\ \frac{(1-p-c)(E-D)}{h(1-p)} + \frac{1-c}{h} \Phi_{\text{sx}} \\ \frac{[1-p-c-h(1-p)](E-D)}{h(1-p)} + \frac{1-c}{h} \Phi_{\text{sx}} \end{bmatrix}, \quad (32)$$

where  $a_{23} = (\rho_s - \rho_w)gh/2\rho - g/(1-p)$ ,  $a_{24} = g/(1-p)$ ,  $\Phi_{\text{sx}} = \partial(h\varepsilon_s \partial c / \partial x) / \partial x$ ,  $\tau_{\text{xx}} = 2\nu_t \partial u / \partial x$ . Other variables are the same as specified earlier. By solution of the eigenvalues of the Jacobian matrix  $\mathbf{A}$  through  $|\mathbf{A} - \lambda \mathbf{I}| = 0$ , we obtain the characteristic speed for mobile-bed case,

$$\lambda_{1,3} = u \mp \sqrt{gh}, \quad (33a)$$

$$\lambda_2 = u, \quad (33b)$$

$$\lambda_4 = 0, \quad (33c)$$

where  $\lambda_{2,4}$  is the sediment- and bed-related characteristic speed. Thus, for the present model of noncapacity sediment transport (equation (30)), the flow-related eigenvalues  $\lambda_{1,3}$  and the maximum local characteristic speed  $\lambda_{\text{sx}}$  in the mobile-bed condition are the same as those for the fixed bed case. This is also demonstrated by Cao *et al.* [2007] using a similar equation system. While the eigenvalues will be also affected by sediment concentration when a capacity sediment transport model is used [De Vries, 1969; Morris and Williams, 1996], this should not be confused with the present work employing the physically more appealing noncapacity modeling approach.

### 3.5. Estimation of Turbulent Eddy Viscosity

[24] Unlike unbounded 2-D flows, the flow pattern in shallow water is strongly influenced by the depth and bed friction [Chen and Jirka, 1995, 1997; Lloyd *et al.*, 2001]. Thus, for 2-D shallow flows, the turbulence model should consider both turbulence generated at the bed and turbulence associated with 2-D horizontal eddies [Uijtewaald and Tukker, 1998]. The depth-averaged mixing length model is intended for such conditions [Jia and Wang, 1999; Cea *et al.*, 2007]. Following this concept, the turbulent eddy viscosity accounting for both the horizontal and vertical production of turbulence is calculated from

$$\nu_t = l_s^2 \sqrt{2S_{ij}S_{ij} + \left( \frac{\kappa u_* h}{6l_s^2} \right)^2} \quad (34)$$

with

$$S_{ij} = \frac{(\partial u_i / \partial x_j + \partial u_j / \partial x_i)}{2}, \quad l_s = C_s \sqrt{\Delta x \Delta y}, \quad (35)$$

where  $S_{ij}$  is the horizontal mean strain-rate tensor;  $u_i$  and  $u_j$  are the depth-averaged velocities;  $x_i$  and  $x_j$  are the horizontal coordinates;  $l_s$  is the characteristic horizontal turbulent length scale;  $C_s$  is the Smagorinsky constant  $\approx 0.16$  for isotropic turbulent flow [Lilly, 1967]; and  $\kappa = 0.41$  is the von Karman constant. The diffusion coefficient for suspended load is simply assumed to be the same as the turbulent eddy viscosity, whereas it is set equal to zero for bedload transport.

### 3.6. Treatment of Wetting and Drying Fronts

[25] When solving the constituting equations with a FVM, it is critical to predict the evolution of wetting and drying fronts in cases such as flood inundation and dam break over a dry bed. Following Zhao *et al.* [1994], we introduce two tolerance depths  $h_{\text{tol1}}$  and  $h_{\text{tol2}}$  ( $h_{\text{tol1}} > h_{\text{tol2}}$ ) for the cell type judgment: dry, partially dry, and wet cells. For a wet cell with the water depth being larger than  $h_{\text{tol1}}$ , the governing equations ((9), (10a), (10b), (10c), (11a), and (11b)) are used. For a partially dry cell, the water depth is between the two specified tolerance depths with the velocity, sediment concentration, and bed level change being set to zero. For a dry cell, the water depth is even smaller than  $h_{\text{tol2}}$  and set to zero together with the velocity, sediment concentration, and bed level change. For a new time interval, a cell changes from dry to wet if water can flow inside from surrounding cells, and from wet to dry if the computed depth is smaller than  $h_{\text{tol2}}$ . The equations for the above treatment of a partially dry cell (see equation (36)) and a dry cell (see equation (37)) are

$$u = v = c = \Delta z = 0, \quad (36)$$

where  $\Delta z$  is the bed change over a time increment.

$$h = u = v = c = \Delta z = 0. \quad (37)$$

### 3.7. Boundary Conditions

[26] The present 2-D model includes two types of boundary conditions, for closed and open boundaries, respectively. At a closed boundary, a free-slip and nonpermeable condition is used. For Cartesian coordinates of  $x$  and  $y$ , this condition reads

$$h_b = h_L, \quad (38a)$$

$$c_b = c_L, \quad (38b)$$

$$\Delta z_b / \Delta t = \Delta z_L / \Delta t, \quad (38c)$$

where the subscripts  $b$  and  $L$  denote the positions of the closed boundary and the adjacent inner cell, respectively. If the closed boundary is along the  $x$  direction, we set  $u_b = u_L$ ,  $v_b = 0$ . Otherwise,  $v_b = v_L$ ,  $u_b = 0$ .

[27] At an open boundary, the fully coupled system for the sediment-laden flow and the riverbed is solved. In subcritical flow condition, the flow and sediment variables are obtained by a modified characteristic method including the second-order Runge-Kutta scheme (see equations (14) and (15)), and the bed level is computed using the bed update equation (5). Unlike the traditional characteristic method

for clear water flow, in which the bed level update is decoupled with the flow computation, the modified version updates the bed level while computing the flow and sediment. For a general form of the compatibility equation along the characteristics,

$$\frac{dw}{dt} = f(w), \quad (39)$$

where  $w$  is the nonconservative variable (i.e.,  $u$  or  $c$ ) along the characteristics, and  $f$  is the source term in the compatibility equation. An example for the exact formulation of  $f$  in the sediment-laden flow is given by Cao *et al.* [2007]. The modified characteristic method within an iterative step reads

$$w^{n+1} = w^n + 0.5(k_1 + k_2) \quad (40)$$

with

$$k_1 = \Delta t f(w^n), k_2 = \Delta t f(w^n + k_1), \quad (41)$$

where  $w^{n+1}$  is the estimate of the variable at the boundary for the new time step, and  $w^n$  is the estimate of the variable along the characteristics (inside the computational domain) for the previous time step. During one iterative step, the bed level is updated by equation (5) using the newly obtained flow and sediment variables after the computation of equation (40). The iteration continues until the difference between two consecutive iterative steps is negligible. We therefore use the computed variables from the last iterative step to approximate the boundary condition for the new time step. This coupling treatment at the open boundaries facilitates a completely synchronous solution of the sediment-laden flow and riverbed in the whole computational domain. Furthermore, it enhances the numerical stability at open boundaries in the case of rapid bed deformation, such as hyperconcentrated floods and mobile-bed dam break.

## 4. Model Test

[28] The present model has been verified by a series of selected test cases, in which the computed results are compared with analytical solutions, experimental data, and other numerical models published in the literature. Five test cases are considered in this paper, viz., (1) 2-D idealized dam break over fixed dry bed, (2) a 2-D dyke-breach experiment on wet fixed bed, (3) idealized dam-break flows over mobile beds, (4) erosional dam-break flow in an abruptly widening channel, and (5) a 2-D partial dam break in a straight mobile-bed channel.

### 4.1. Case 1: 2-D Idealized Dam Break Over Fixed Dry Bed

[29] Many laboratory experiments have been performed for dam-break flows over fixed beds [Fraccarollo and Toro, 1995; Stelling and Duinmeijer, 2003; Ferrari *et al.*, 2010]. To verify the model's ability for flooding over a fixed dry bed, the experiment conducted by Fraccarollo and Toro [1995] is simulated. The experimental flume consisted of an upstream reservoir of 1 m  $\times$  2 m and a

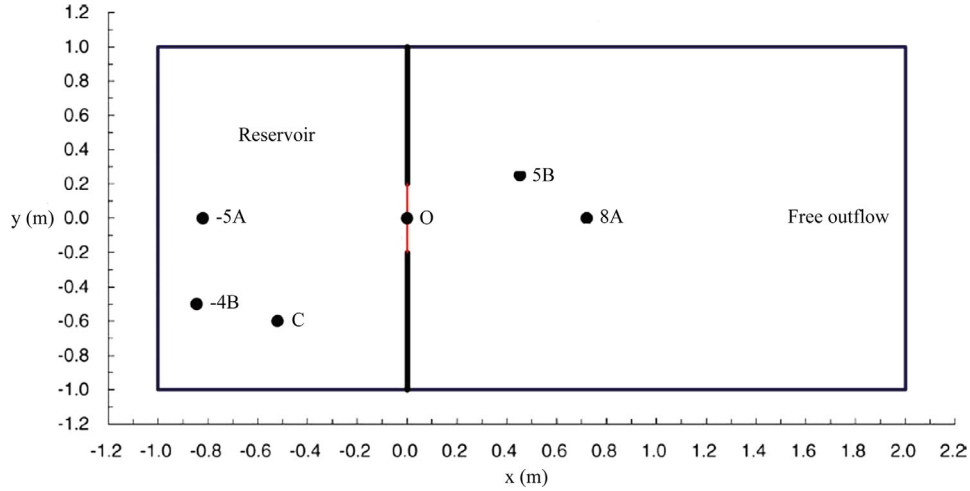


**Figure 1.** Sketch of the idealized dam-break experiment (m).

downstream floodplain of  $2\text{ m} \times 2\text{ m}$  (see Figure 1). A  $0.4\text{ m}$  wide breach was located in the middle of the downstream boundary of the reservoir. For the present test the flume was horizontal, and the bottom friction was negligible. The dam break was initiated with upstream  $0.6\text{ m}$  deep water flowing over a downstream dry bed. Measuring gauges were installed at distinct locations (see Figure 1): O  $(0, 0)$ , -5A  $(-0.82, 0)$ , 8A  $(0.722, 0)$ , C  $(-0.52, -0.6)$ , 5B  $(0.454, 0.25)$ , and -4B  $(-0.845, -0.5)$ .

[30] The computation lasts for  $10\text{ s}$  with grid cells of  $0.02\text{ m} \times 0.02\text{ m}$  and the CFL condition of  $Cr=0.45$ , based on a convergence study. Closed boundary conditions are imposed at all solid edges of the reservoir and free outflow at the three open boundaries of the downstream floodplain. The two tolerance depth for judging the dry and partially dry cells are set to  $0.0001$  and  $0.0002\text{ m}$ .

[31] Figure 2 shows good agreement between the computed and measured water levels above the fixed bed at

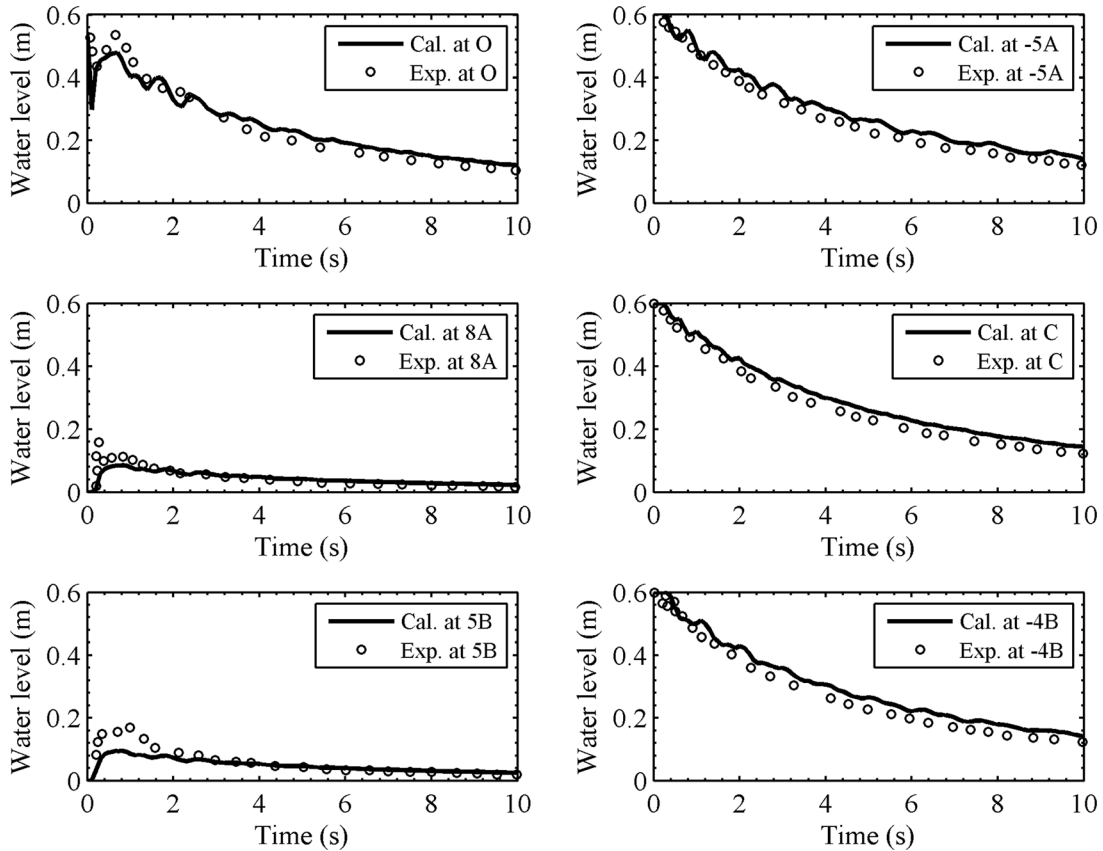


**Figure 2.** Comparison of computed (solid lines) and measured (circles) water level history at distinct gauges.

distinct gauges. At the breach (i.e., gauge O), the model captures the phenomenon of falling and rising stages at the beginning of the dam break. Inside the reservoir, the lowering of water level due to a depression wave is also well reproduced by the present model (see gauges -5A, -4B, C). In the downstream region, the model satisfactorily predicts the wavefront at gauge 8A, while it computes much lower water level in the early 2 s at gauge 5B. This could be caused by the measuring method that the water level was obtained from pressure meters at gauge 5B while directly measured by wave height meters at other gauges [Fraccarollo and Toro, 1995]. In general, the model is capable of capturing the key features of 2-D dam-break flow over a dry bed.

#### 4.2. Case 2: 2-D Dyke Breach Over Horizontal Fixed Bed

[32] Case 2 is the wet bed dyke-breach experiment undertaken in the Fluid Mechanics Laboratory at Delft University of Technology [Stelling and Duinmeijer, 2003]. In this test case, the influences of the gate opening and the effects of breach contraction are not negligible, which causes more complexity and difficulty in numerical modeling.

[33] The test flume contained a flat fixed bed with an area of 31.4 m × 8 m. The dam was a solid wall at  $x = 2.5$  m and had a 0.4 m wide gate opening in the middle (see Figure 3). The initial water depth inside the upstream reservoir was 0.6 m, and 0.05 m in the downstream region. Measuring gauges were installed along the flume centerline and numbered in sequence (G0–G5) by specific distances from the gate opening, -1, 1, 6, 9, 13, and 17 m. At the start of the experiment, the gate was opened by lifting the door at a speed of 0.16 m/s.

[34] The relatively slow movement of the gate door requires a special treatment until the gate is fully opened. Following Liang *et al.* [2004], the discharge at the gate is calculated using the formula for submerged culvert flow:

$$q = C_w h_w \sqrt{2g(H - C_w h_w)}, \quad (42)$$

where  $q$  is the flow discharge ( $\text{m}^2/\text{s}$ ),  $H$  is the headpond water depth (taken equal to the water depth of the grid cell immediately upstream of the gate),  $h_w$  is the gate opening height, and  $C_w$  is the contraction coefficient ( $=0.9$ ). When the gate is completely opened, the local head loss due to the sudden contraction is taken into account by incorporating an extra resistance stress [Zhou *et al.*, 2002] immediately upstream of the opening:

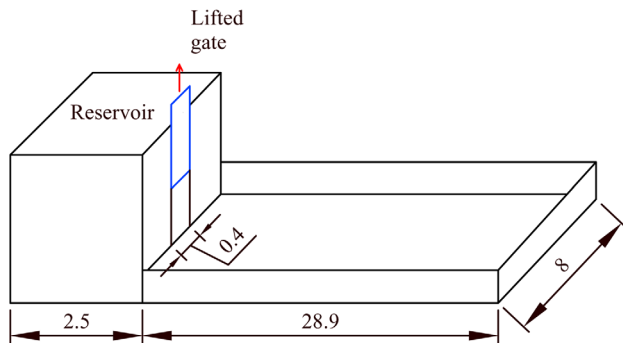


Figure 3. Sketch of the dyke-breach experiment (m).

$$\tau_{\xi x} = -\xi u_g \sqrt{u_g^2 + v_g^2}, \quad (43a)$$

$$\tau_{\xi y} = -\xi v_g \sqrt{u_g^2 + v_g^2}, \quad (43b)$$

where  $\tau_{\xi x(y)}$  is the resistance stress in  $x$  ( $y$ ) directions,  $\xi = 0.8$ , and  $u_g, v_g$  are the velocities in the  $x$  and  $y$  directions at the breach, respectively.

[35] The computation lasts for 25 s with grid cells of 0.1 m × 0.1 m and the CFL condition of  $Cr = 0.45$ , based on a convergence study. Closed boundary conditions are imposed at all solid edges. The Manning roughness coefficient is set at 0.012 for the wet bed [Stelling and Duinmeijer, 2003].

[36] The numerical results of the present 2-D coupled model agree closely with those published by others [Stelling and Duinmeijer, 2003; Liang *et al.*, 2004, 2006; Cui *et al.*, 2010]. Figure 4 shows good agreement between the computed and measured wavefront positions at  $t = 1, 2, 3,$  and 4 s. The wavefront is predicted slightly faster near the downstream side wall of the dyke and along the flume centerline. This is probably because the wall friction and the influence of a piece of plastic along the centerline are not considered in the current modeling.

[37] Figure 5 shows the 3-D view and the contour plots of the computed water surface at distinct instants. In the early stage of the dyke breach (e.g.,  $t = 4$  s, see Figure 5a), a shock wave is observed propagating downstream with a semicircular wavefront heading a water mass of almost constant depth. This water mass is then followed by a hydraulic jump, which is pushed downstream by the strength of high-speed flow from the gate opening. Reflective waves are observed when the wavefront hits the lateral walls. As time proceeds, the wavefront becomes nearly straight with curved bore-reflection waves behind as shown in Figure 5b, due to the complex interactions between the reflective waves and the initial waves. The hydraulic jump still exists in the later stage but migrates downstream at a much lower speed than the wavefront.

[38] As shown in Figure 6, the computed water depth agrees generally well with the experiment data at different gauges along the centerline. Particularly, the magnitude and arrival time of the first flood wave are well simulated at all gauges downstream of the breach. Yet less accurate

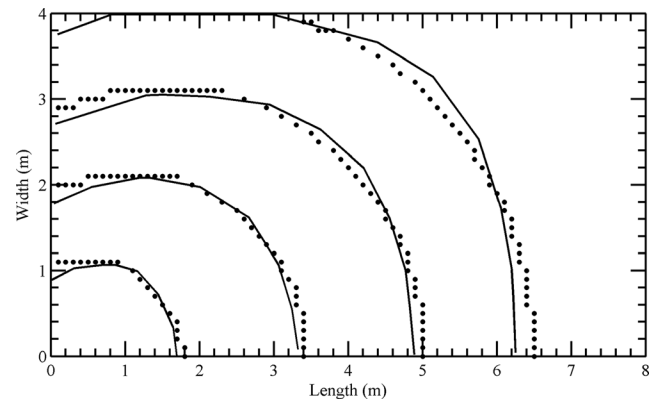
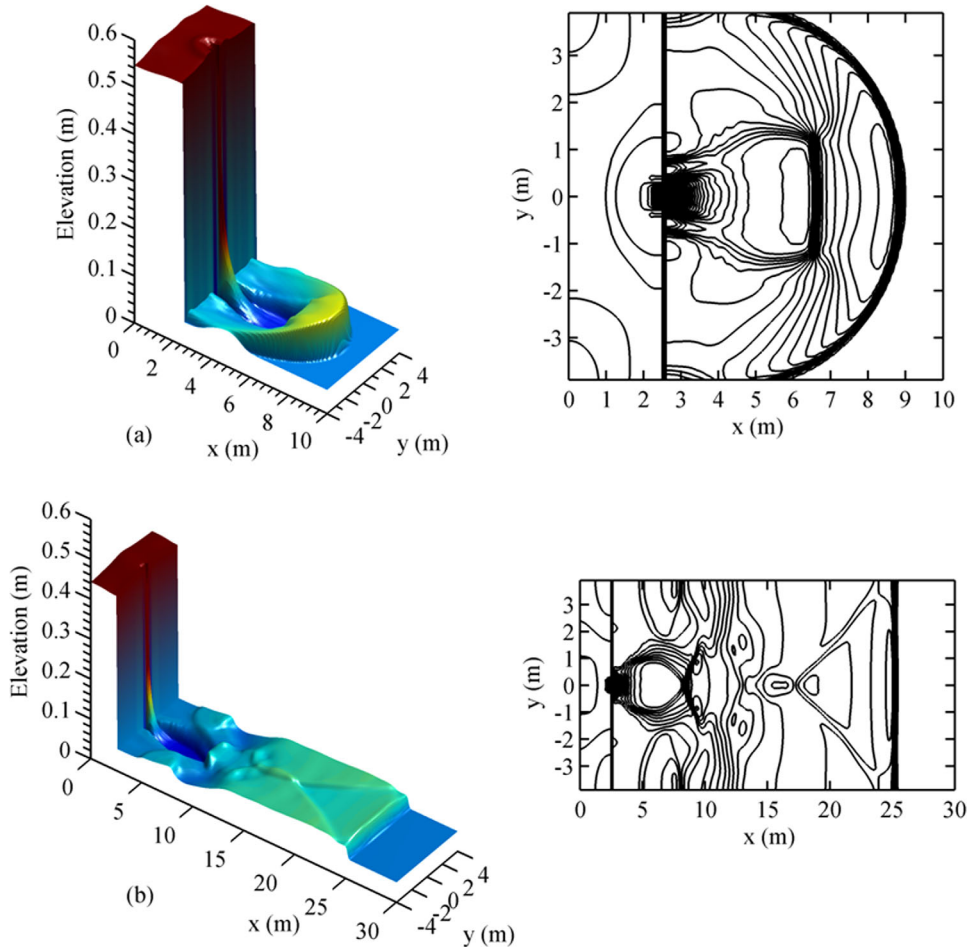


Figure 4. Comparison of computed (dots) and measured (solid lines) wavefront positions over the wet bed at  $t = 1, 2, 3, 4$  s.



**Figure 5.** Free surface and contours for wet bed case at (a)  $t = 4$  s and (b)  $t = 18$  s.

results are predicted for the second flood wave. In the immediate downstream of the breach (i.e., gauge 1), the water level is overpredicted after the first flood wave. This probably causes the underprediction of the magnitude and speed of the second flood wave in the downstream. Moreover, the treatment of the gate opening and contraction effects is quite empirical in the model, uncertainties are inevitable. With increasing distance, the accumulative effect of bed friction further slows down the second wave propagation. But in general, the model result is satisfactory and in similar trend of accuracy with other published models [Stelling and Duinmeijer, 2003; Liang et al., 2004, 2006].

#### 4.3. Case 3: Idealized Dam-Break Flows Over Mobile Beds

[39] To verify the model's hydromorphological modeling performance, two sets of idealized tests on dam-break flow over a mobile bed are numerically investigated. These tests comprise the experiments carried out in Taipei (University of Taiwan) and Louvain-la-Neuve (Université Catholique de Louvain (UCL)), reported by Capart and Young [1998] and Fraccarollo and Capart [2002], respectively. The two experiments were both performed in horizontal prismatic flumes of rectangular cross sections but differ primarily in the sediment material used. In the Taipei experiment, the flume was 1.2 m long, 0.2 m wide, and 0.7 m

high. It was initially covered by a 5 to 6 cm thick layer of light artificial pearls (not natural sand), of a diameter of 6.1 mm, specific gravity of 1.048, and settling velocity of 0.076 m/s. In the Louvain experiment, the flume was 2.5 m long, 0.1 m wide, and 0.35 m high. Cylindrical polyvinyl chloride pellets (not natural sand) having a diameter of 3.2 mm, height of 2.8 mm (hence, an equivalent spherical diameter of 3.5 mm), specific gravity of 1.54, and settling velocity of 0.18 m/s constituted an initial sediment layer of 5 to 6 cm thick over the fixed bottom. In both experiments, an idealized dam was located in the middle of the flume separating an upstream static flow region of 10 cm deep from a dry downstream part. At  $t = 0$  s, the dam was lifted rapidly to create the dam-break flow.

[40] For the numerical simulation of both tests, the domain is divided into grid cells of  $0.0025 \text{ m} \times 0.0025 \text{ m}$ , and the Courant number in the CFL condition is 0.3 based on a convergence study. The simulation time is 0.6 s and 1.2 s for the Taipei and Louvain tests, respectively. Following Wu and Wang [2007], the bed porosity is set at 0.28 and 0.3 in the Taipei and Louvain tests, respectively, while the Manning roughness coefficient of 0.025 is used for both. For the sediment entrainment/deposition, the threshold Shields parameter  $\theta_c$  is set at 0.15 and 0.05 in the Taipei and Louvain tests, respectively [Li and Duffy, 2011]. The submerged specific gravity of sediment  $s$  is calculated as

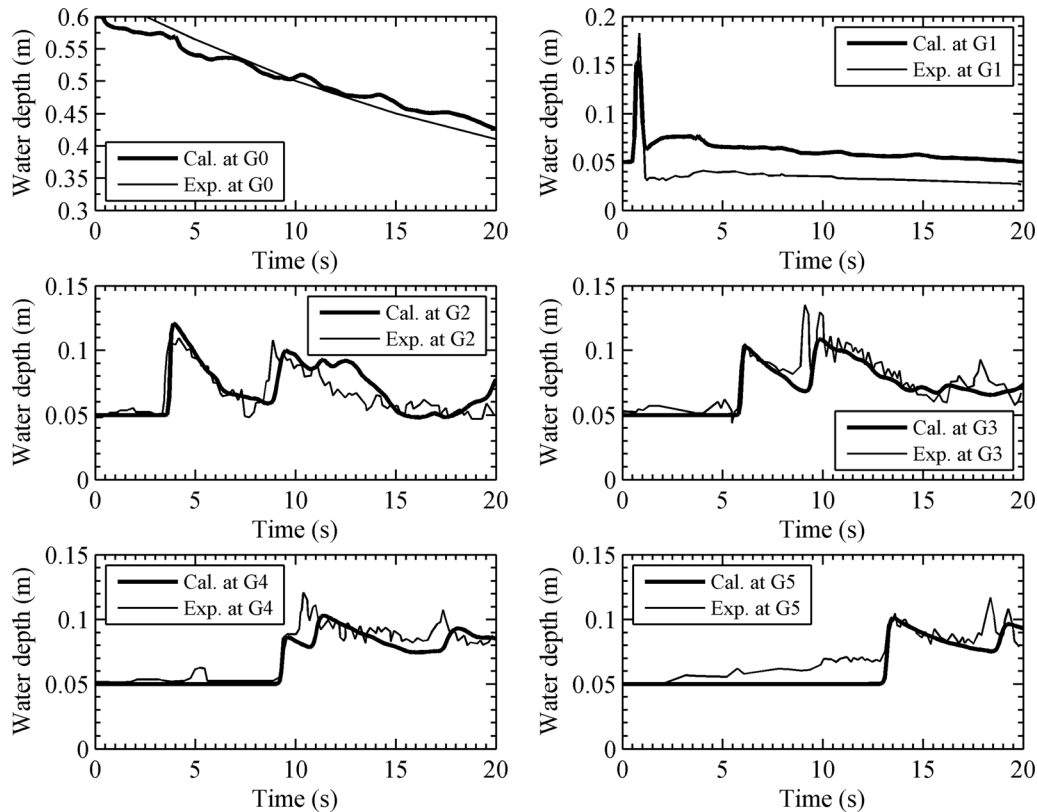


**Figure 6.** Comparison of computed (thick line) and measured (thin line) water depth histories over wet bed at distinct gauges.

0.048 and 0.54 for the Taipei and Louvain tests, respectively. Trial runs give values of other parameters:  $\alpha = 3$ ,  $\varphi = 6$  in the Taipei test, and  $\alpha = 3$ ,  $\varphi = 3$  in the Louvain test.

[41] Based on a number of assumptions (i.e., capacity sediment transport, a constant concentration in sediment moving layers, zero momentum loss due to bed friction, etc.), pseudoanalytical solutions of free surface and bed evolution were derived by *Fraccarollo and Capart* [2002] for both tests. In Figures 7 and 8 the computed results at varying times are compared with those analytical solutions in nondimensional self-similar coordinates where experimental data are also shown. For both tests, good agreement is generally observed between the simulation and measurement while to some parts the analytical solution exhibits qualitative discrepancies from them.

[42] For the Taipei test (see Figure 7), the agreement among the simulation, analytical solution, and measurement is fairly good for the wavefront location, the erosion magnitude, and the downstream (adverse) slope of the scour hole. Yet considerable differences appear in the upstream (downward) slope of the scour hole and the water surface. Along the upstream slope of the scour hole, erosion is somewhat underestimated by the numerical simulation while excessively overestimated by the analytical solution, as compared to the experiment. The hydraulic jump occurring near the dam-break location can be qualitatively captured by the simulation, though with less accurate prediction of its location. In contrast, the analytical solution shows a constant water level and fails to predict this phenomenon. For the front water surface, the computed and an-

alytical results are very close and agree well with the measured data. The backwater surface can be satisfactorily predicted by the simulation but less well by the analytical solution.

[43] For the Louvain test (see Figure 8), better agreement is observed among the computed, analytical, and measured results. The measured water surface and bed level are satisfactorily predicted in the numerical simulation. The location of the hydraulic jump is well reproduced by the numerical model for this test, where both computed and measured results show the hydraulic jump propagates upstream. The location of wavefront and erosion magnitude are also modeled well in the simulation. Though the analytical solution shows great resemblance to the simulation and measurement in the erosion magnitude as well as in the front- and backwater surface, it again cannot predict the hydraulic jump and obviously overestimates the wavefront propagation.

[44] To understand the causes of those differences, some critical issues should be addressed. First, comparing with the simulation based on the noncapacity sediment transport, the failure to reproduce the hydraulic jump with the analytical solution may be mainly caused by the assumption of the capacity sediment transport. This echoes the previous suggestions by *Capart and Young* [1998] and *Fraccarollo and Capart* [2002] that the central wave region is the most sensitive to nonequilibrium behavior. Moreover, the nonhydrostatic pressure, which is not considered in both numerical simulation and analytical analysis, may also have some influence [*Fraccarollo and Capart*, 2002]. Second, the

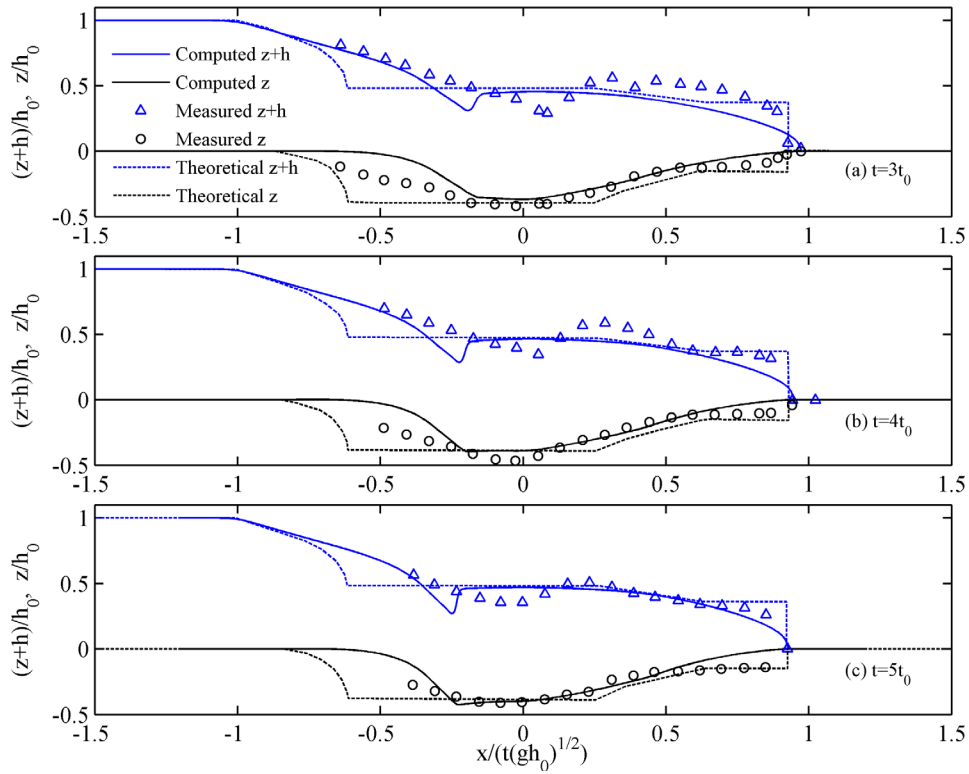


**Figure 7.** Comparison of computed water surface and bed level with pseudoanalytical solution [Fracarollo and Capart, 2002] and data from the Taipei experiment.

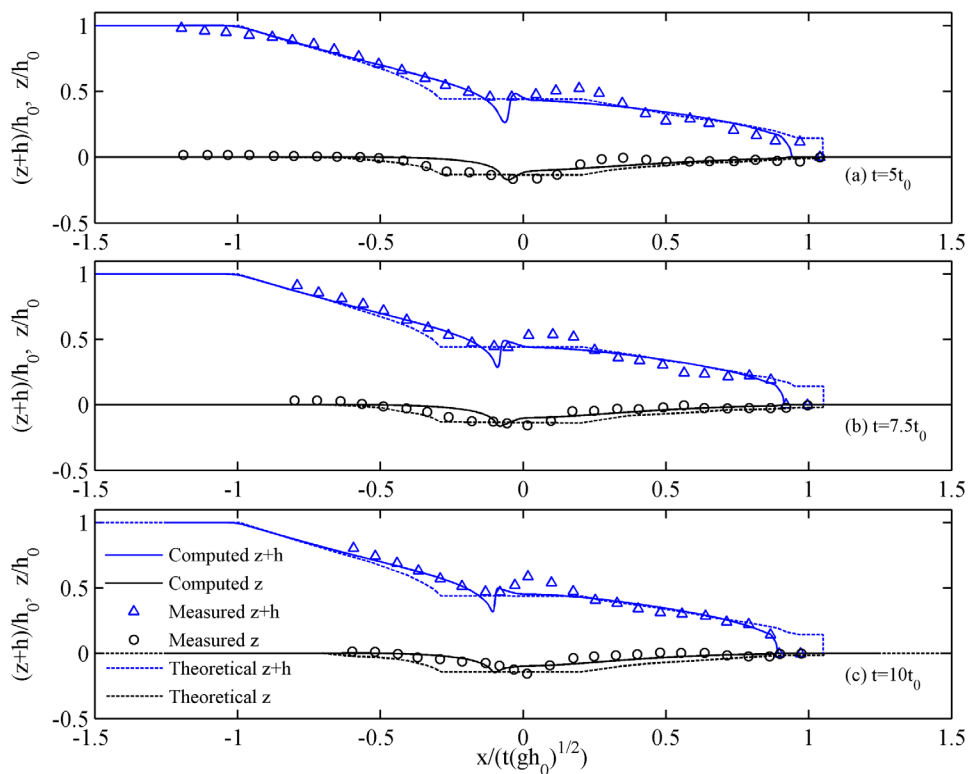


**Figure 8.** Comparison of computed water surface and bed level with pseudoanalytical solution [Fracarollo and Capart, 2002] and data from the Louvain experiment.

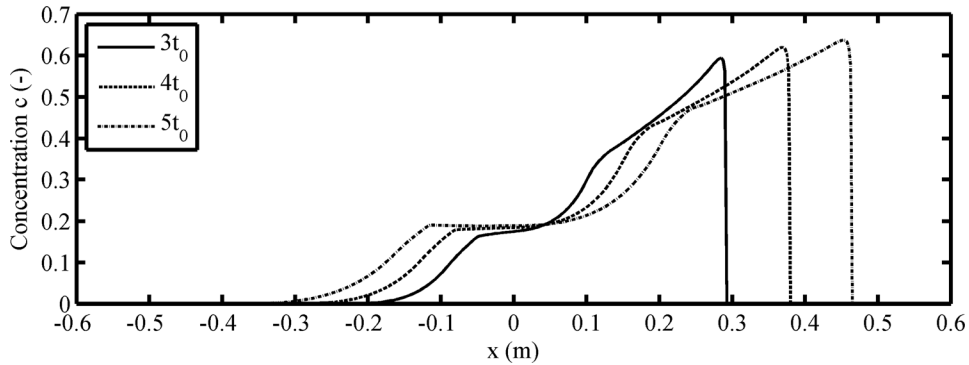


**Figure 9.** Computed volumetric sediment concentration for the Taipei experiment.

faster propagation of the wavefront in the analytical solution for late times (see the Louvain test in Figure 8) is probably due to the assumption of zero momentum loss from bed friction. Practically, the dissipative effect due to bed friction becomes important and slows down the bore movement when time evolves [Fraccarollo and Capart, 2002]. Third, the less satisfactory analytical solution in the Taipei test is attributed to the use of light particle material, which makes the theory of capacity sediment transport less appropriate for this case [Fraccarollo and Capart, 2002]. Fourth, the assumption of a constant concentration in the sediment moving layer is another flaw in the analytical derivation [Cao *et al.*, 2004; Wu and Wang, 2007], which could result in less accurate predictions. But in general, the pseudoanalytical solution agrees qualitatively well with the measurement for the idealized tests and can serve as an alternative reference for the model test.

[45] To shed light on the model’s capacity of modeling high sediment concentrations, the computed longitudinal concentrations in the Taipei test are drawn for distinct time instants (see Figure 9). The model is stable at very high sediment concentrations (e.g.,  $c_{\max} \approx 0.64$  at  $5t_0$ ) under relatively strong erosive conditions. Steep concentration gradient can be well captured by the model. The computed profile and magnitude at  $4t_0$  are very close to those simulated by Wu and Wang [2007].

#### 4.4. Case 4: Erosional Dam-Break Flow in an Abruptly Widening Channel

[46] Laboratory-scale experiments of dam break over an erodible bed were conducted at the Civil Engineering Laboratory of the UCL, Belgium [Spinewine and Zech, 2007; Palumbo *et al.*, 2008; Zech *et al.*, 2008; Goutiere *et al.*,

2011]. The experiment considered here was conducted in a 6 m long flume, with a sudden asymmetric enlargement from 0.25 to 0.5 m in the downstream reach (see Figure 10). A 0.1 m high layer of saturated sand with diameter of  $d = 1.82$  mm and density of  $\rho_s = 2680$  kg/m<sup>3</sup> constituted the initial flat bed with bed porosity of  $p = 0.47$ . At the downstream end of the flume, a weir was installed to allow a free outflow. The dam break was initiated instantaneously by rapidly moving down a thin gate at the middle of the flume, allowing the water contained in the upstream reservoir ( $h_0 = 0.25$  m) pouring into the downstream dry bed. Measurements of water level history and final bed topography were carried out at specific gauges and cross sections [Palumbo *et al.*, 2008]. Gauges 1–4 were located along the line  $y = 0.125$  m, with  $x = 3.75$ , 4.2, 4.45, and 4.95 m, respectively. Gauges 5 and 6 were in line of  $y = 0.375$  with  $x = 4.2$  and 4.95 m. The two cross sections are along  $x = 4.1$  m (CS1) and  $x = 4.4$  m (CS2).

[47] Based on a convergence study, the computational domain is discretized into grid cells of  $\Delta x = 0.025$  m and  $\Delta y = 0.005$  m, and the Courant number in the CFL condition is 0.45. The total computational time is 12 s with the time step controlled by the stability condition (19). Free outflow condition is imposed at the downstream boundary, while the closed boundary condition is used for all side walls. For sediment entrainment and deposition computation, equations (7a), (7b), (8a), and (8b) are used with specified parameters:  $\theta_c = 0.04$ ,  $\alpha = 10$ ,  $\varphi = 0.5$ , and  $s = 1.68$ . The Manning roughness coefficient is  $0.024$  m<sup>-1/3</sup>/s, and this value refers to those used by others [Zech *et al.*, 2008; Xia *et al.*, 2010; Wu *et al.*, 2012]. The two tolerance depths in dry/wet front treatment are set to 0.0001 and 0.0002 m, respectively.

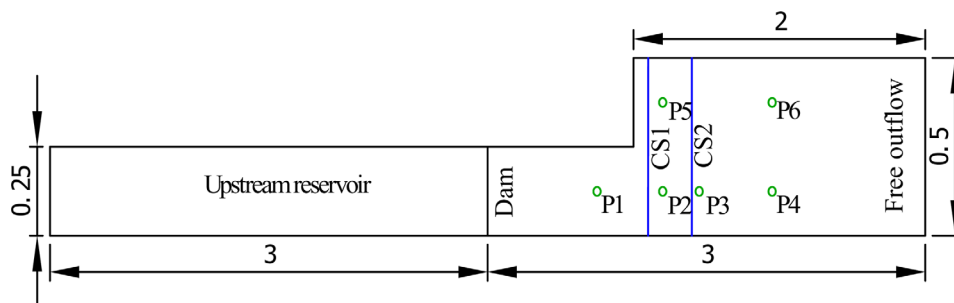


**Figure 10.** Sketch of the UCL dam-break experiment in a widening channel (m).

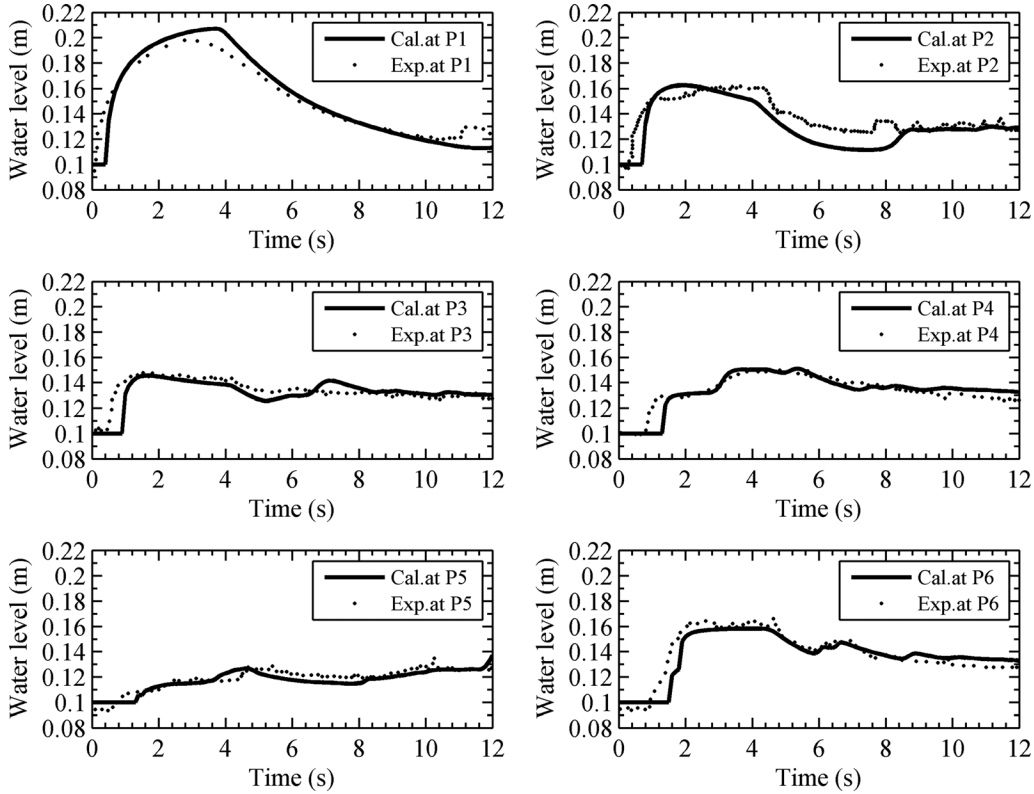


**Figure 11.** Comparison between computed (thick line) and measured (dots) water level at distinct gauges.

[48] The present 2-D coupled model yields results of similar accuracy as those predicted by triangular/rectangular meshes and upwind methods such as Roe-MUSCL, HLLC, or HLL schemes [Palumbo *et al.*, 2008; Xia *et al.*, 2010; Soares-Frazaõ and Zech, 2011; Wu *et al.*, 2012]. Figure 11 shows the comparison between the computed and measured water level histories at distinct gauges. The computed results agree well with those measured at gauges 1, 3, 4, 5, and 6, but they are less close in the narrow part (gauge 2) immediately downstream of the enlargement. Specifically, relatively low water level was predicted at gauge 2 immediately after the flood peak (around 4–8 s) along with a possible overestimation of local bed erosion.

This should be attributed to the sudden change of domain related the enlargement, where the flow and bed change computation are very sensitive and rather difficult to track.

[49] Figure 12 shows the computed final bed changes in the immediate downstream of the sudden enlargement. At the cross section CS1, the model can reproduce the bed erosion at the center of the flume near the corner of the enlargement but underestimates the deposition at the enlarged zone (Figure 12a). At CS2, the measured bed profile of moderate erosion in the narrow part and strong deposition in the enlarged zone (Figure 12b) is reproduced, but the erosion magnitude is slightly overpredicted in the narrow part. The local erosion near the sidewall of the enlarged zone (at the

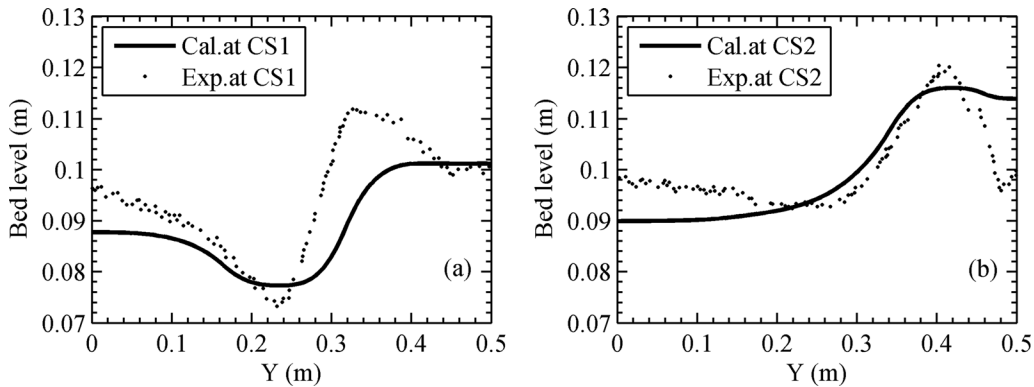


**Figure 12.** Comparison of computed (thick line) and measured (dots) bed profiles at (a) CS1 and (b) CS2.

far right sides of Figures 12a and 12b) is most probably caused by vertical recirculation (observed by *Palumbo et al.* [2008]), which however cannot be adequately represented by a depth-averaged model.

#### 4.5. Case 5: Partial Dam Break in a Straight Erodeable Channel

[50] Case 5 is a mobile-bed dam-break experiment that was also conducted in UCL-Belgium [*Wu et al.*, 2012; *Soares-Frazão et al.*, 2012]. The flume was 3.6 m wide and about 36 m long (Figure 13). A 1 m wide gate between two impervious blocks represented the dam-break location, with the gate center denoting the coordinate (0,0). The mobile bed had a 0.085 m high layer of saturated sand with diameter of  $d = 1.61$  mm and density of  $\rho_s = 2630$  kg/m<sup>3</sup>, which extended from 1 m upstream of the gate to 9 m downstream with bed porosity of  $p = 0.42$ . The downstream end of the flume consisted of a weir and sediment entrapment system. The initial water level is 0.47 m (above the fixed flat bed) upstream of the gate and 0 m in the downstream region (dry bed case). The partial dam break was modeled by rapidly lifting the gate and lasted for 20 s. Measurements of water surface and bed level were conducted in two repeated experiment runs for the above experimental setup. Water surface measurements were undertaken at eight gauges during both experiment runs. Gauges 1–4 were located along  $x = 0.64$  m, with  $y = -0.5, -0.165, 0.165,$  and  $0.5$  m, respectively. Gauges 5–8 were along  $x = 1.94$  m, with  $y = -0.99, -0.33, 0.33,$  and  $0.99$  m, respectively. Bed measurements were carried out at the end of the two experiments ( $t = 20$  s), with data available for three longitudinal lines ( $y = 0.2, 0.7,$  and  $1.45$  m).

[51] Based on a convergence study, the computational domain is discretized into grid cells of  $\Delta x = \Delta y = 0.025$  m, and the Courant number in the CFL condition is 0.45. The total computational time is 20 s with the time step controlled by the stability condition (19). Transmissive conditions are imposed at the downstream boundary due to the

relatively short experiment period, and closed boundaries at walls are free-slip and nonpermeable. The sediment entrainment and deposition are computed by equations (7a), (7b), (8a), and (8b), with specified parameters:  $\theta_c = 0.04$ ,  $\alpha = 5$ ,  $\varphi = 1$ , and  $s = 1.63$ . The bed roughness is 0.0165 for sand layer and 0.01 for fixed bed portion [*Wu et al.*, 2012]. The tolerance depths in dry/wet front treatment are 0.001 and 0.0005 m, respectively.

[52] Figure 14 shows the comparison of the computed and measured water level histories (above the fixed flat bed) at eight gauges. The difference between the two measurements for the same experimental setup indicates the difficulty of repeating such experiments. At the symmetric gauges (viz., 1(4), 2(3), 5(8), 6(7)), the computed water level changes are exactly the same indicating the model's accuracy in the symmetric property of  $y$  direction. At gauges 5(8) and 6(7), the computed results agree well with the experiment data. In the near-downstream region of the dam, less accurate results are predicted. At gauges 1 and 4, the water level is underpredicted in the early stage of the dam break, while it is overpredicted at gauges 2 and 3 near the centerline.

[53] Figure 15 shows the predicted bed profiles against the experiment data along three longitudinal lines ( $y = 0.2, 0.7,$  and  $1.45$  m) at the end of the experiment ( $t = 20$  s). Considerable discrepancies between the two groups of measured bed profile (with the same experimental setup) are observed especially in the near downstream of the breach. It indicates the bed change near the dam region is very sensitive and unstable even to trivial disturbances in doing the experiments. In this region, the predicted bed erosion along  $y = 0.2$  and  $0.7$  m is between the two measurements, while the deposition along  $y = 1.45$  m is underpredicted. In the far downstream region where close agreement is observed between the two measurements, the accuracy of the predicted bed level is also much improved.

[54] The less accurate prediction for both water level and bed profile in the near downstream of the breach may relate

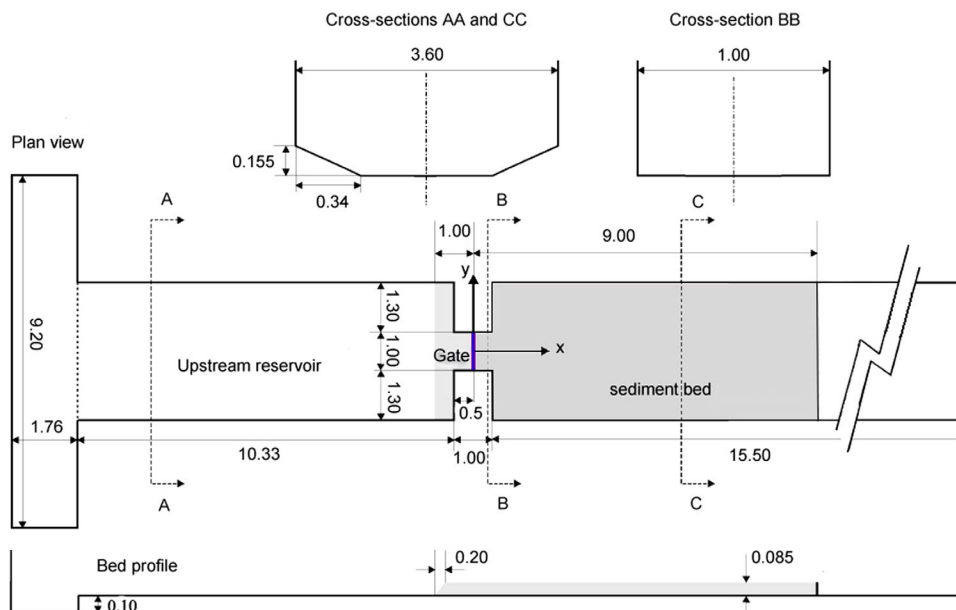
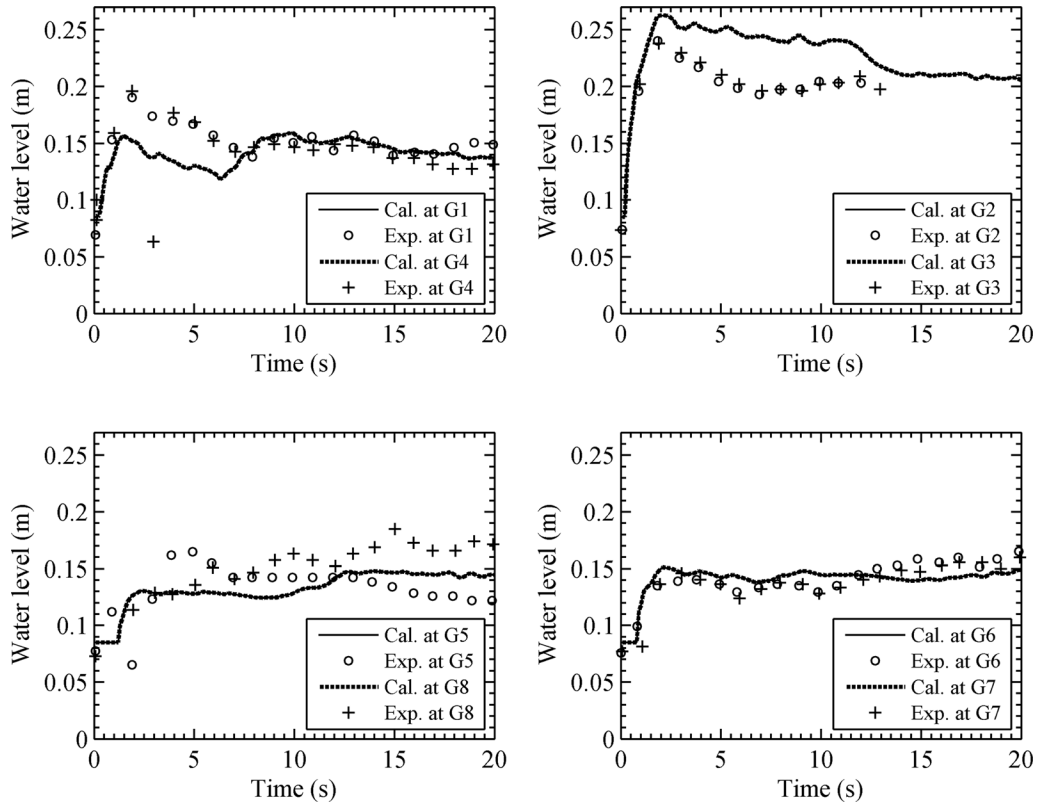
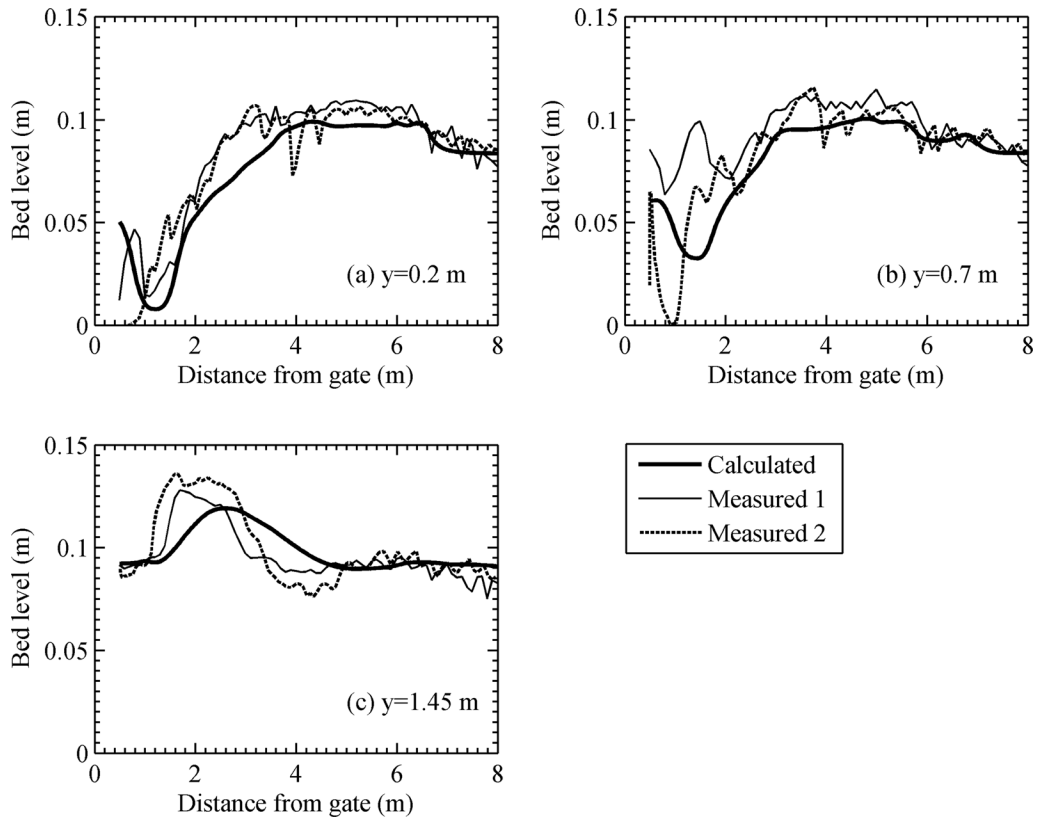


Figure 13. Sketch of the UCL partial dam-break experiment (m).



**Figure 14.** Comparison between computed and measured water levels at distinct gauges.



**Figure 15.** Comparison between computed and measured bed profiles along different longitudinal lines.

to the strong 3-D flow features around the corners of the expansion which cannot be fully considered in a depth-averaged model. At the early stage, less flow is computed to expand laterally (see gauges 1 and 4), while more flow concentrates along the centerline (see gauges 2 and 3). The uncertainty in bed change prediction for this sensitive area may affect the water level computation as well. Yet considering the complexity of the problem, the model results are generally well and should be considered acceptable.

## 5. Conclusions

[55] An accurate and efficient 2-D depth-averaged model has been developed under the framework of the fully coupled noncapacity modeling approach. This has been achieved by the successful extension of the second-order UFORCE method (developed by *Stecca et al.* [2010]) from the idealized frictionless-fixed bed case to the mobile-bed case. The combination of the upwind and centered methods in the UFORCE scheme leads to high accuracy and computational efficiency in the present model, which is absent in previous fully coupled and noncapacity models.

[56] In solving the equation set, synchronous procedure is deployed with flow, sediment, and bed computed simultaneously. An explicit two-stage splitting approach [*Toro, 2001*] together with a second-order Runge-Kutta method is used for the inhomogeneous system. The model is second-order accurate in space and time. At the open boundary, a modified characteristic method is adopted, which incorporates the above Runge-Kutta method and the morphological update in each iterative cycle of flow (sediment) computation. This treatment enhances the model stability and permits a complete synchronous and fully coupled solution in the entire computational domain.

[57] The model has been verified against five test cases, which cover a wide range of complex flow and sediment transport conditions, including two fixed bed dam-break tests and three mobile-bed tests. The model is demonstrated to be capable of simulating not only shock waves and reflection waves but also rapid bed deformations under highly active sediment transport conditions. The extension of the UFORCE scheme to the sediment-laden flow over a mobile bed is less computationally demanding than most upwind methods, while offering attractive efficiency and satisfactory accuracy.

[58] In practical applications, such as flood forecasting, flood risk and river basin management, and river channel restoration, efficient and accurate solutions are favored in order to cope with the large spatial scales involved. The combination of high numerical accuracy and computational efficiency by the present work makes the present model a promising tool for such applications. Yet it should be pointed out that for highly irregular bed topographies and complex boundaries, the modeling accuracy and efficiency depend on both the numerical method and the computational grid. For such conditions, the absence of C-property (in still water conditions) and the use of rectangular grid in the present model may reduce the modeling accuracy and efficiency. Further development to incorporate a well-balanced scheme and a more flexible mesh-cell like triangular cell or adaptive quadtree grid is part of future work.

[59] While uncertainty related to empirical and numerical parameters of the model is inevitable, reasonable agree-

ment between numerical solutions and experimental data can be obtained if those parameters are sensibly specified. Also, the values of the parameters used in the present numerical cases may be only applicable to the experimental configurations of the specific case. For further applications of morphological models, it is important to collect as much information as possible for the targeted configuration so that sensible values of parameters can be given.

## Notation

The following symbols are used in this manuscript:

$\mathbf{A}$	Jacobian matrix.
$\mathbf{F}, \mathbf{G}$	vectors of flux variables.
$\mathbf{H}$	vector of source terms.
$\mathbf{I}$	vector of diffusive terms.
$\mathbf{K}_1, \mathbf{K}_2$	vectors defined in equation (15).
$\mathbf{R}, \mathbf{R}'$	vector of total source terms.
$\mathbf{U}$	vector of conservative variables.
$\mathbf{W}$	vector of nonconservative variables.
$c, c_e$	depth-averaged volumetric sediment concentration and capacity, respectively.
$c_{\max}$	maximum sediment concentration.
$C_s$	Smagorinsky constant.
$C_w$	contraction coefficient.
$Cr$	Courant number.
$d$	sediment diameter.
$E, D$	sediment entrainment and deposition fluxes.
$f$	function in characteristic method.
$g$	acceleration of gravity.
$H$	headpond water depth.
$h, h_0$	water depth.
$h_w$	gate opening height.
$i, j$	cell indices in the coordinate of $x$ and $y$ directions.
$k_1, k_2$	variables defined in equation (41) in characteristic method.
$l_s$	characteristic horizontal turbulent length scale.
$n$	Manning roughness coefficient.
$p$	bed porosity.
$Pe$	Peclet number.
$q$	flow discharge defined in equation (42).
$q_b$	bed load transport rate under capacity state.
$s$	submerged specific gravity of sediment.
$S_{0x}, S_{0y}$	bed slopes in $x$ and $y$ directions.
$S_{fx}, S_{fy}$	friction slopes in $x$ and $y$ directions.
$S_{ij}$	horizontal mean strain-rate tensor.
SIG	function defined in equation (27).
$t$	time.
$u_*$	friction velocity.
$u, v$	depth-averaged flow velocities in $x$ and $y$ directions.
$u_g, v_g$	velocities in equation (43a).
$w$	variable in characteristic method.
$x, y$	horizontal coordinates.
$z$	bed elevation.
$\tau_{xx}, \tau_{yy}, \tau_{xy}, \tau_{yx}$	depth-averaged Reynolds stresses.
$\tau_{\xi x(y)}$	resistance stress in $x$ ( $y$ ) directions.
$\xi$	parameter in equation (43b).

$v_t$	turbulent eddy viscosity.
$\Phi_s$	sediment diffusion term.
$\varepsilon_s$	turbulent diffusion coefficient of sediment.
$\rho_s, \rho_w$	densities of sediment and water, respectively.
$\rho$	density of sediment-laden flow.
$\rho_0$	density of saturated bed.
$\varphi$	modified parameter in equation (8a).
$\theta, \theta_c$	Shields parameter.
$\alpha$	empirical coefficient.
$\omega$	sediment settling velocity.
$\phi$	newly constructed conservative variable in equation (10a).
$\Delta x, \Delta y$	spatial steps in $x$ and $y$ directions.
$\Delta t$	time step.
$\frac{\Delta z}{\Delta x}$	bed level change.
$\Delta_j$	vector of limited slope.
$\beta_x$	upwind bias parameter in UFORCE scheme.
$\kappa$	von Karman constant.
$\lambda$	characteristic speed.

[60] **Acknowledgments.** This research is sponsored by the China Scholarship Council (2008621194) and supported by the Sino-Dutch collaboration project “Effects of human activities on the eco-morphological evolution of rivers and estuaries” (08-PSA-E-01) funded by the Royal Dutch Academy of Sciences (KNAW) and the Chinese Ministry of Science and Technology (MOST) within the framework of the Programme of Scientific Alliances between China and Netherlands. Also, the authors very much appreciate the anonymous reviewers for their constructive comments that improved this paper.

## References

- Alcrudo, F., and P. Garcia-Navarro (1993), A high-resolution Godunov-type scheme in finite volumes for the 2D shallow-water equations, *Int. J. Numer. Methods Fluids*, 16(6), 489–505.
- Bradford, S. F., and B. F. Sanders (2002), Finite-volume model for shallow water flooding of arbitrary topography, *J. Hydraul. Eng.*, 128(3), 289–298.
- Canestrelli, A., M. Dumbser, A. Siviglia, and E. F. Toro (2010), Well-balanced high-order centered schemes on unstructured meshes for shallow water equations with fixed and mobile bed, *Adv. Water Resour.*, 33, 291–303.
- Cao, Z. X., G. Pender, S. Wallis, and P. Carling (2004), Computational dam-break hydraulics over erodible sediment bed, *J. Hydraul. Eng.*, 130(7), 689–703.
- Cao, Z. X., Y. T. Li, and Z. Y. Yue (2007), Multiple time scales of alluvial rivers carrying suspended sediment and their implications for mathematical modeling, *Adv. Water Resour.*, 30, 715–729.
- Cao, Z. X., Z. J. Li, G. Pender, and P. Hu (2012), Non-capacity or capacity model for fluvial sediment transport, *Water Manage.*, 165(WM4), 193–211.
- Capart, H., and D. L. Young (1998), Formulation of a jump by the dam-break wave over a granular bed, *J. Fluid Mech.*, 372, 165–187.
- Cea, L., J. Puertas, and M. Vázquez-Cendón (2007), Depth averaged modelling of turbulent shallow water flow with wet-dry fronts, *Arch. Comput. Methods Eng.*, 14, 303–341.
- Chen, D. Y., and G. H. Jirka (1995), Experimental study of plane turbulent wakes in a shallow water layer, *Fluid Dyn. Res.*, 16, 11–41.
- Chen, D. Y., and G. H. Jirka (1997), Absolute and convective instabilities of plane turbulent wakes in a shallow water layer, *J. Fluid Mech.*, 338, 157–172.
- Cui, H. Y., J. D. Pietrzak, and G. S. Stelling (2010), A finite volume analogue of the  $P_1^{NC} - P_1$  finite element: with accurate flooding and drying, *Ocean Model.*, 35, 16–30.
- Cui, Y., C. Paola, and G. Parker (1996), Numerical simulation of aggradation and downstream fining, *J. Hydraul. Res.*, 34(2), 185–204.
- Cunge, J. A., F. M. Holly, and A. Verwey (1980), *Practical Aspects of Computational River Hydraulics*, Pitman, London.
- De Vries, M. (1969), Solving river problems by hydraulic and mathematical models, paper presented at the Conference on Selected Problems from the Theory of Simulation of Hydrodynamic Phenomena, Jablonna, Poland.
- Di Cristo, C., M. Iervolino, and A. Vacca (2006), Linear stability analysis of a 1-D model with dynamical description of bed-load transport, *J. Hydraul. Res.*, 44(4), 480–487.
- Egashira, S., N. Honda, and T. Itoh (2001), Experimental study on the entrainment of bed material into debris flow, *Phys. Chem. Earth C*, 26(9), 645–650.
- Ferrari, A., L. Fraccarollo, M. Dumbser, E. F. Toro, and A. Armanini (2010), Three-dimensional flow evolution after a dam-break, *J. Fluid Mech.*, 663, 456–477.
- Fraccarollo, L., and H. Capart (2002), Riemann wave description of erosional dam-break flows, *J. Fluid Mech.*, 461, 183–228.
- Fraccarollo, L., and E. F. Toro (1995), Experimental and numerical assessment of the shallow water model for two-dimensional dam-break type problems, *J. Hydraul. Res.*, 33, 843–864.
- Garegnani, G., G. Rosatti, and L. Bonaventura (2011), Free surface flows over mobile bed: Mathematical analysis and numerical modeling of coupled and decoupled approaches, *Commun. Appl. Ind. Math.*, 1–22, doi:10.1685/journal.caim.371.
- Godunov, S. K. (1959), A difference method for the numerical calculation of discontinuous solutions of hydrodynamic equations, *Mat. Sbornik*, 47(3), 271–306 (JPRS).
- Goutiere, L., S. Soares-Frazão, and Y. Zech (2011), Dam-break flow on mobile bed in a channel with sudden widening: Experimental data, *J. Hydraul. Res.*, 49(3), 367–371.
- Harten, A., B. Engquist, S. Osher, and S. Chakravarthy (1987), Uniformly high order accuracy essentially non-oscillatory schemes. III, *J. Comput. Phys.*, 71, 231–303.
- Heng, B. C. P., G. C. Sander, and C. F. Scott (2009), Modeling overland flow and soil erosion on nonuniform hillslopes: A finite volume scheme, *Water Resour. Res.*, 45, W05423, doi:10.1029/2008WR007502.
- Hu, P., and Z. X. Cao (2009), Fully coupled mathematical modeling of turbidity currents over erodible bed, *Adv. Water Resour.*, 32(1), 1–15.
- Hu, P., Z. X. Cao, G. Pender, and G. M. Tan (2012), Numerical modelling of turbidity currents in the Xiaolangdi reservoir, Yellow river, China, *J. Hydrol.*, 464, 41–53.
- Jia, Y. F., and S. S. Y. Wang (1999), Numerical model for channel flow and morphological change studies, *J. Hydraul. Eng.*, 125(9), 924–933.
- Julien, P. Y. (2010), *Erosion and Sedimentation*, 2nd ed., Cambridge Univ. Press, Cambridge, UK.
- Lax, P. D. (1954), Weak solutions of nonlinear hyperbolic equations and their numerical computation, *Commun. Pure Appl. Math.*, VII, 159–193.
- Lesser, G. R., J. A. Roelvink, J. A. T. M. van Kester, and G. S. Stelling (2004), Development and validation of a three-dimensional morphological model, *Coastal Eng.*, 51, 883–915.
- Li, S. C., and C. J. Duffy (2011), Fully coupled approach to modeling shallow water flow, sediment transport, and bed evolution in rivers, *Water Resour. Res.*, 47, W03508, doi:10.1029/2010WR009751.
- Liang, D. F., R. A. Falconer, and B. L. Lin (2006), Comparison between TVD-MacCormack and ADI-type solvers of the shallow water equations, *Adv. Water Resour.*, 29, 1833–1845.
- Liang, Q. H., A. G. L. Borthwick, and G. S. Stelling (2004), Simulation of dam- and dyke-break hydrodynamics on dynamically adaptive quadtree grids, *Int. J. Numer. Methods Fluids*, 46, 127–162.
- Lilly, D. K. (1967), The representation of small-scale turbulence in numerical simulation experiments, paper presented at IBM Scientific Computing Symposium on Environmental Sciences, Tomas J. Watson Res. Cent., Yorktown Heights, N. Y.
- Lloyd, P. M., P. K. Stansby, and D. Y. Chen (2001), Wake formation around islands in oscillatory laminar shallow water flows. Part 1: Experimental investigation, *J. Fluid Mech.*, 429, 217–238.
- Meyer-Peter, E., and R. Müller (1948), Formulas for bed-load transport, paper presented at the 2nd Meeting of International Association for Hydraulic Structures Research, Int. Assoc. for Hydraul. Struct. Res., Stockholm.
- Morris, P. H., and D. J. Williams (1996), Relative celerities of mobile bed flows with finite solids concentrations, *J. Hydraul. Eng.*, 122(6), 311–315.
- Palumbo, A., S. Soares-Frazão, L. Goutiere, D. Pianese, and Y. Zech (2008), Dam-break flow on mobile bed in a channel with a sudden enlargement, paper presented at River Flow 2008 International Conference on Fluvial Hydraulics, IAHR-Fluvial Hydraul. Comm., Izmir-Cesme, Turkey.

- Phillips, B. C., and A. J. Sutherland (1989), Spatial lag effects in bed load sediment transport, *J. Hydraul. Res.*, 27(1), 115–133.
- Roe, P. L. (1981), Approximate Riemann solvers, parameter vectors and difference schemes, *J. Comput. Phys.*, 43, 357–372.
- Rosatti, G., and L. Fraccarollo (2006), A well-balanced approach for flows over mobile-bed with high sediment-transport, *J. Comput. Phys.*, 220, 312–338.
- Sieben, J. (1999), A theoretical analysis of discontinuous flow with mobile bed, *J. Hydraul. Res.*, 37(2), 199–212.
- Simpson, G., and S. Castelltort (2006), Coupled model of surface water flow, sediment transport and morphological evolution, *Comput. Geosci.*, 32, 1600–1614.
- Soares-Frazão, S., and Y. Zech (2011), HLLC scheme with novel wave-speed estimators appropriate for two-dimensional shallow-water flow on erodible bed, *Int. J. Numer. Methods Fluids*, 66, 1019–1036.
- Soares-Frazão, S., et al. (2012), Dam-break flows over mobile beds: Experiments and benchmark tests for numerical models, *J. Hydraul. Res.*, 50(4), 364–375.
- Spinewine, B., and Y. Zech (2007), Small-scale laboratory dam-break waves on movable beds, *J. Hydraul. Res.*, 45, 73–86.
- Stecca, G., A. Siviglia, and E. F. Toro (2010), Upwind-biased FORCE schemes with applications to free-surface shallow flows, *J. Comput. Phys.*, 229, 6362–6380.
- Stelling, G. S., and S. P. A. Duijnmeijer (2003), A staggered conservative scheme for every Froude number in rapidly varied shallow water flows, *Int. J. Numer. Methods Fluids*, 43, 1329–1354.
- Toro, E. F. (2001), *Shock-Capturing Methods for Free-Surface Shallow Flows*, John Wiley, England.
- Toro, E. F. (2009), *Riemann Solvers and Numerical Methods for Fluid Dynamics: A Practical Introduction*, 3rd ed., Springer, Berlin.
- Uijtewaal, W. S. J., and J. Tukker (1998), Development of quasi two-dimensional structures in a shallow free-surface mixing layer, *Exp. Fluids*, 24, 192–200.
- Van Leer, B. (1979), Towards the ultimate conservative difference scheme. V: A second order sequel to Godunov’s method, *J. Comput. Phys.*, 32(2), 101–136.
- Wu, W. M., and S. S. Y. Wang (2007), One-dimensional modeling of dam-break flow over movable beds, *J. Hydraul. Eng.*, 133(1), 48–58.
- Wu, W. M., and S. S. Y. Wang (2008), One-dimensional explicit finite-volume model for sediment transport with transient flows over movable beds, *J. Hydraul. Res.*, 46(1), 87–98.
- Wu, W. M., W. Rodi, and T. Wenka (2000), 3D numerical modeling of flow and sediment transport in open channels, *J. Hydraul. Eng.*, 126(1), 4–15.
- Wu, W. M., R. Marsooli, and Z. G. He (2012), Depth-averaged two-dimensional model of unsteady flow and sediment transport due to noncohesive embankment break/breaching, *J. Hydraul. Eng.*, 138(6), 503–516.
- Xia, J. Q., B. L. Lin, R. A. Falconer, and G. Q. Wang (2010), Modelling dam-break flows over mobile beds using a 2D coupled approach, *Adv. Water Resour.*, 33, 171–183.
- Zech, Y., S. Soares-Frazão, B. Spinewine, and N. Le Grelle (2008), Dam-break induced sediment movement: experimental approaches and numerical modelling, *J. Hydraul. Res.*, 46(2), 176–190.
- Zhang, R. J., and J. H. Xie (1993), *Sedimentation Research in China-Systematic Selections*, China Water Power Press, Beijing.
- Zhao, D. H., H. W. Shen, G. Q. Tabios III, J. S. Lai, and W. Y. Tan (1994), Finite-volume two-dimensional unsteady-flow model for river basins, *J. Hydraul. Eng.*, 120(7), 863–883.
- Zhou, J. G., D. M. Causon, D. M. Ingram, and C. G. Mingham (2002), Numerical solutions of the shallow water equations with discontinuous bed topography, *Int. J. Numer. Methods Fluids*, 38, 769–788.